



HAL
open science

High-Resolution Lagrangian Inverse Modeling of CO₂ Emissions Over the Paris Region During the First 2020 Lockdown Period

K. Nalini, Thomas Lauvaux, C. Abdallah, J. Lian, Philippe Ciais, H. Utard,
O. Laurent, Michel Ramonet

► **To cite this version:**

K. Nalini, Thomas Lauvaux, C. Abdallah, J. Lian, Philippe Ciais, et al.. High-Resolution Lagrangian Inverse Modeling of CO₂ Emissions Over the Paris Region During the First 2020 Lockdown Period. *Journal of Geophysical Research: Atmospheres*, 2022, 127 (14), pp.e2021JD036032. 10.1029/2021jd036032 . hal-03738503

HAL Id: hal-03738503

<https://hal.science/hal-03738503v1>

Submitted on 26 Jul 2022

HAL is a multi-disciplinary open access archive for the deposit and dissemination of scientific research documents, whether they are published or not. The documents may come from teaching and research institutions in France or abroad, or from public or private research centers.

L'archive ouverte pluridisciplinaire **HAL**, est destinée au dépôt et à la diffusion de documents scientifiques de niveau recherche, publiés ou non, émanant des établissements d'enseignement et de recherche français ou étrangers, des laboratoires publics ou privés.

JGR Atmospheres

RESEARCH ARTICLE

10.1029/2021JD036032

Key Points:

- Quantification and mapping of fossil fuel CO₂ emissions over the Paris metropolitan area during the COVID-19 pandemic lockdown
- Lockdown has resulted in an emission decrease of about 43% in 2020, with a 37% contribution from the inventory itself
- Spatial error correlations, different background conditions and prior uncertainty impact the posterior emission estimates

Correspondence to:

K. Nalini,
naliniks91@gmail.com

Citation:






Nalini, K., Lauvaux, T., Abdallah, C., Lian, J., Ciais, P., Utard, H., et al. (2022). High-resolution Lagrangian inverse modeling of CO₂ emissions over the Paris region during the first 2020 lockdown period. *Journal of Geophysical Research: Atmospheres*, 127, e2021JD036032. <https://doi.org/10.1029/2021JD036032>

Received 12 OCT 2021
Accepted 28 JUN 2022

Author Contributions:

Conceptualization: K. Nalini, T. Lauvaux
Data curation: O. Laurent, M. Ramonet
Formal analysis: K. Nalini
Funding acquisition: T. Lauvaux
Investigation: K. Nalini
Methodology: K. Nalini, T. Lauvaux
Resources: T. Lauvaux, C. Abdallah, J. Lian, H. Utard, O. Laurent, M. Ramonet
Software: T. Lauvaux, C. Abdallah, J. Lian
Supervision: T. Lauvaux
Validation: K. Nalini
Writing – original draft: K. Nalini
Writing – review & editing: K. Nalini, T. Lauvaux, C. Abdallah, J. Lian, P. Ciais, M. Ramonet

High-Resolution Lagrangian Inverse Modeling of CO₂ Emissions Over the Paris Region During the First 2020 Lockdown Period

K. Nalini^{1,2} , T. Lauvaux¹, C. Abdallah¹ , J. Lian^{1,3} , P. Ciais¹ , H. Utard³, O. Laurent¹, and M. Ramonet¹ 

¹Laboratoire des Sciences du Climat et de l'Environnement, LSCE/IPSL, CEA-CNRS-UVSQ, Université Paris-Saclay, Gif-sur-Yvette, France, ²School of Meteorology, University of Oklahoma, Norman, OK, USA, ³SUEZ, Le Pecq, France

Abstract Stringent mobility restrictions across the world during the COVID 19 pandemic have impacted local economies and, consequently, city carbon budgets, offering a unique opportunity to evaluate the capability of scientific approaches to quantify emissions changes. Our study aims to quantify and map CO₂ emissions from fossil fuel and biogenic CO₂ fluxes over the Paris metropolitan area during the first lockdown period (March-May 2020) in France, in comparison with the same period in 2019. Our inversion system relies on transport model simulations initiated with the Weather Research and Forecasting chemistry transport model combined with a high-resolution fossil fuel CO₂ emissions inventory, and biogenic CO₂ fluxes from a vegetation model. The inversion with atmospheric observations from a network of six towers resulted in a positive re-adjustment of fossil fuel CO₂ emissions in 2019 and 2020 compared to prior. In 2020, the inversion resulted in a large emission reduction (43%) compared to 2019, while the reductions were estimated to be 37% based on the prior inventory itself. By assimilating CO mixing ratios in addition to CO₂, the *traffic* emission estimates were reduced by 68% in 2020, compared to *nontraffic* (29%). Various sensitivity tests show that prior emission uncertainty and different background conditions significantly impacted the emissions estimates. We conclude that our current inversion system with atmospheric CO₂ monitoring makes it possible to identify the emission decrease in 2020 partly over the urban region. However, additional information on prior emission errors and a dense network will be needed to map emissions precisely.

Plain Language Summary The study aims to quantify the Paris region's CO₂ emissions using a Lagrangian-based inversion system during the spring season (March-May) of 2019–2020, using CO₂ and co-emitted CO observations from a network of six ground-based stations. Our Inversion system tends to increase the emissions with respect to prior in 2019 and 2020. A significant increase (about 150 g CO₂ m⁻² day⁻¹) in the fossil fuel emissions compared to prior was identified in the central Paris region across all our inversion experiments. Sectoral inversion shows an increase in the traffic emissions from the high-resolution inventory by about 17% in 2019 and 10% in 2020. However, the impact of COVID 19 lockdown on the emissions were –37% to –46% (reduction) depending on the configuration of the inversion system. We also identified that the lack of information relative to inventory uncertainties remains a major limitation in quantifying the aggregated emissions. Precise mapping of fossil fuel emissions at the urban scale will require additional information to quantify both the high-resolution inventory errors and their spatial structures. However, we confirmed the impact of lockdown restrictions on CO₂ fossil fuel emissions to –12% ({plus minus}4%) over the Paris region through inversion.

1. Introduction

Climate change caused by increased atmospheric greenhouse gas (GHG) mixing ratios has been accelerating since the dawn of industrialization (Pachauri et al., 2014). Among the various sources of GHGs, urban areas contribute more than half to the emissions of fossil-fuel carbon dioxide (CO₂) (Roest et al., 2020) on the global scale and are expected to increase as the global population and urbanization grow (Seto et al., 2014). A reliable and robust approach to reporting accurate urban emissions is needed to design and implement efficient mitigation strategies (Hsu et al., 2019). Conventionally, bottom-up approaches often referred to as emissions inventories, are used to estimate GHG emissions based on activity data and emission factors at national and sub-national scales (e.g., IPCC, 2006). Recent studies have shown that despite well-established protocols and standards, urban-scale

inventory estimates tend to omit specific sectors of activities due to limited data access and tend to use outdated emission factors, resulting in systematic under-estimation of city emissions (e.g., Gurney et al., 2021). The multiplicity of protocols and approaches (Arioli et al., 2020) combined with regular updates of emission factors and standards results in major discrepancies when tracking emission changes over the years (Mueller et al., 2021).

Atmospheric transport models representing the atmospheric processes act as the backbone of the inverse modeling technique (Enting, 2002). The atmospheric inversion approach relies on CO₂ mixing ratio measurements from buildings or towers within and around a city or aircraft has been studied over several metropolitan areas (e.g., Paris (Bréon et al., 2015), Indianapolis (Lauvaux et al., 2016) and Los Angeles (Feng et al., 2016)). These studies have demonstrated the success of inversion to quantify urban CO₂ emissions at annual to 3-year timescales for large cities (e.g., Bréon et al., 2015; Lauvaux et al., 2016; Nickless et al., 2018; Oda et al., 2017; Staufer et al., 2016). More recent studies have also demonstrated that tower-based inversion can detect and quantify short-term city-wide emissions changes during the recent COVID 19 lockdown periods (Lian et al., 2022; Yadav et al., 2021).

Two sectors of activities, that is, residential/commercial and transport, consume the largest fraction of fossil fuel energy in urban areas (Pataki et al., 2006). In addition, point emission sources such as power plants make the concentration plume highly variable (Bréon et al., 2015). However, CO₂ emitted from these sources mixes rapidly with other sources and sinks before being transported outside the city limits by the wind. Therefore, the estimation of CO₂ fluxes in the city needs to consider observations from within and around the city (McKain et al., 2012). Fossil fuel emissions are the dominant source of CO₂ in an urban area, whereas, in rural remote locations, the biogenic influence (net ecosystem exchange) dominates the observed variations (Miles et al., 2021). Biogenic sources can partially offset the emissions during the growing season, even at the urban scale, depending on the green vegetation fraction and the regional ecosystems (Miller et al., 2020; Staufer et al., 2016). The ability of the vegetation models to reproduce the regional biogenic fluxes mostly comes from the highly heterogeneous vegetation (depending on the land cover), impacted by human interventions (Gourdji et al., 2022). Radio-isotopic tracers such as ¹⁴C (Turnbull et al., 2015) or eddy-covariance flux towers (Wehr et al., 2013) have revealed significant contributions from urban vegetation. For example, the role of parks and gardens in residential areas to the observed variations in CO₂ mixing ratios over Los Angeles have been discussed by Miller et al., 2020. Based on a ¹⁴CO₂ measurement campaign, Lopez et al. (2013) found the biospheric contribution of 23% in the total CO₂ emissions in Paris in wintertime.

The inversion is impacted by sources of uncertainties associated with the atmospheric transport model (Geels et al., 2012) and unreliability in prior emission representation (Lauvaux et al., 2016). Other uncertainties such as representation errors arise from the differences between point measurements and transport model grid boxes (Gerbig et al., 2003) or aggregation errors due to the inability to separate various sources in a single grid cell (Kaminski et al., 2001). At the city scale, spatial and temporal granularity in prior emissions is represented by proxies prone to large uncertainties (Super et al., 2021) or due to large local point sources (e.g., industries, power plants). Fine-scale (~1 km) atmospheric transport modeling needs to account for urban heat island effects (Pal et al., 2012), urban landscape geometries impacting the local dynamics, and heterogeneous surface characteristics (Bréon et al., 2015; Hutyra et al., 2014).

The city of Paris is relatively flat and is densely populated with high emission intensity. Earlier inversion studies implemented over the Paris region to estimate urban CO₂ emissions (Bréon et al., 2015; Staufer et al., 2016) were based on the CHIMERE transport model at a spatial resolution of 16 × 16 km. These studies demonstrated that atmospheric gradients provided a sufficient constraint on fossil fuel emissions to estimate annual emissions within 10 Mt CO₂. Noticeable observation-model mismatches in CO₂ mixing ratios remained, even after the optimization, due to the variability in background conditions and potential errors in atmospheric transport. More recently, Lian et al. (2021) examined the Weather Research and Forecasting (WRF-Chem) model performances at higher resolution (1 km) over the Paris region with improved model performances in simulating CO₂ gradients influenced by the local atmospheric dynamics and emissions.

The use of additional atmospheric tracer species has been studied for separating atmospheric CO₂ signals into components (e.g., Wong et al., 2015). Among them, carbon monoxide (CO) is the most widely used because of its ease of measurement and knowledge of its sources and sinks (Nathan et al., 2018). CO is co-emitted with CO₂ due to the incomplete combustion of fossil fuels (Potosnak et al., 1999), primarily from vehicles (Meijer

et al., 1996; Turnbull et al., 2015). Therefore, utilizing the molar ratio of CO:CO₂ can improve fossil fuel CO₂ emission estimates between traffic and nontraffic sectors. Other sources of CO include wildfires and the atmospheric oxidation of methane and non-methane volatile organic compounds (VOC) (Oney et al., 2017) that varies depending on the season and location (e.g., Duncan et al., 2007; Griffin et al., 2007). However, in regional-scale inversions, CO emitted from methane oxidation can be neglected due to the slow rate of oxidation compared to advection over urban area (Holloway et al., 2000). Similarly, VOCs contribute only about 7% and 15% of the global CO source (Duncan et al., 2007) but in summer, oxidation of VOCs can result in large quantities of urban CO, most likely from biogenic sources (Guenther et al., 1995; Miller et al., 2012; Turnbull et al., 2006; Vimont et al., 2019). Hence, CO emitted from vehicles dominates other sources, especially in the winter season and can be used to separate fossil fuel CO₂ emissions from various other sectors (Colvile et al., 2001). Studies by Lopez-Coto et al., 2020 and Super et al. (2017) shows that CO:CO₂ emission ratios could provide an additional constraint on the fossil fuel-generated CO₂. In addition, other atmospheric tracer species such as ¹⁴CO₂ (Levin et al., 2003; Turnbull et al., 2015), δ¹³C (Newman et al., 2016), SF₆ (Maiss & Brenninkmeijer, 1998) and HFC-125 (Velders et al., 2009) are used to separate emissions from different sub-sectors. Over the Paris region, Ammoura et al. (2016) proposed an approach to estimate reliable CO:CO₂ ratios using atmospheric mixing ratio measurements. The ratios exhibited spatial and seasonal variability within the city. The difference in emissions between summer and winter seasons in the study suggested that in addition to traffic, residential heating is also a major source of CO, which is not in agreement with the Airparif inventory (Airparif, 2013). Ammoura et al. (2014) studied the M^oquet tunnel in Thiais, a peri-urban area about 15 km south of Paris center. By evaluating the ratios between CO₂ and co-emitted species, they found a good agreement between the local inventory and the observed CO:CO₂ ratios. Spatial and temporal variabilities in the ratios imply that traffic does not have a unique imprint on the urban plume but rather leaves various signatures, depending on traffic speed and vehicle types. Consolidating these aspects, CO measurements can provide an additional source of information to estimate fossil-fuel CO₂ emissions, but this approach is limited by the uncertainty and space-time variability of CO:CO₂ emission ratios (Kort et al., 2013; Levin & Karstens, 2007; Lopez et al., 2013; Rayner et al., 2014).

Apart from the traditional inversion approach, the Lagrangian-based inversion approach is one of the widely used methods for flux estimation. It provides the sensitivity of individual concentration measurements to all upwind sources with lesser computational simulations than their Eulerian counterparts (Lin et al., 2003). The present study, Lagrangian-based inversion quantifies urban CO₂ emissions and biogenic fluxes over the Paris region during the first lockdown period of 2020 (March–May) and the same period in 2019, using high-accuracy in situ tower measurements of CO₂ mixing ratios. Hourly CO₂ mixing ratio gradients from six towers in and around the Paris urban area are assimilated to produce 5-day mean day-time estimates of fossil fuel CO₂ emissions and biogenic fluxes. Incorporating the gradients helps to eliminate the variability of CO₂ due to the transport of fluxes from remote regions (Bréon et al., 2015). In the second part of the study, to separate traffic CO₂ emissions from other sectors, CO mixing ratios from these sites are jointly assimilated in the inversion. Section 2 summarizes the data and methodology utilized in the present study. Results are described in Section 3, followed by a discussion in Section 4 with different sensitivity tests and conclusions in Section 5.

2. Data and Methodology

2.1. Inverse Methodology

Bayesian inverse modeling provides a top-down technique for verifying the emission and uptake of GHGs (Kaminski et al., 1999; Rayner et al., 1999) by combining a priori information with observations using Bayes' theorem (Enting, 2002). The Inversion mainly requires three components: (1) mixing ratio measurements (2) prior knowledge of fluxes and (3) an operator connecting fluxes/emissions to the measured mixing ratios. This operator is considered linear for long-lived species (such as CO₂) that do not undergo any chemical reactions in the atmosphere. In the Bayesian method, atmospheric observations and a priori information are described in terms of their probability density functions (Heimann & Kaminski, 1999; Tarantola, 1987). These three components, together with their uncertainties, provide the best estimates of fluxes/emissions. Several global scale studies (Bousquet et al., 1999; Ciais et al., 2010; Gurney et al., 2002, 2003; Kaminski et al., 1999; Law et al., 2003; Peylin et al., 2002; Rayner et al., 1999, 2008) and city-scale flux estimation studies (Bréon et al., 2015; Lauvaux et al., 2016; Stauder et al., 2016) utilized Bayesian inversion methodology to estimate emissions/fluxes.

The atmospheric CO₂ mixing ratio observed at a location comprised of surface fluxes/emissions and a background mixing ratio (assumed constant over the domain but varying in time) coming from distant sources/sinks. The mixing ratio observations (c) include information from both local and distant sources. Hence, time-varying background mixing ratios must be subtracted based on atmospheric observations sampled upwind of the city, assuming that (a) they remain fairly constant across the domain, and (b) the simulated influence of local sources/sinks remains small compared to the urban enhancements.

Considering the linear relationship between observations and fluxes, which holds for passive tracers, a cost function can be defined, which consists of mismatches between modeled and observed mixing ratios and the mismatch between prior (known) and posterior (unknown) fluxes along with their respective uncertainties. Minimizing the cost function with respect to the unknown fluxes gives optimized solutions to the surface fluxes (posterior fluxes) (f) and posterior covariance matrix, defined as

$$f = f_0 + C_{f0} H^T (H C_{f0} H^T + C_c)^{-1} (y - H f_0) \quad (1)$$

and

$$C_f = (H^T C_c^{-1} H + C_{f0}^{-1})^{-1} \quad (2)$$

here, f_0 is the prior fluxes, C_{f0} is the error variance-covariance matrix of prior fluxes, H is the Jacobian matrix with each element representing the sensitivity of observations to each component of f (Enting, 2002), C_c is the error variance-covariance matrix of observations, y is the observed mixing ratios and $H f_0$ is the modeled mixing ratios (Tarantola, 2005).

The present study aims to constrain terrestrial fluxes (5-day mean) over the Paris metropolitan area. Prior fluxes and uncertainties are defined at 1 km resolution over a domain of dimension 90 × 90 km. With two emissions/flux sectors averaged over 5-days over the day-time (7–17 UTC), the size of the state vector f is 90 × 90 × 2 (=16,200 unknowns). At the same time, the observation vector consists of hourly afternoon (12–17 UTC) observations (tower gradients) across six sites (one background), reaching a maximum of 6 × 5 × 5 (150) mixing ratio observations. As the advection of air masses across the domain takes less than 5 hr, with the observation time being 12 UTC, the correction to the emissions applies only to daytime emissions starting from 7 UTC.

In addition, percentage error reduction has been determined to quantify the theoretical improvement in posterior fluxes compared with prior. The error reduction U_R is defined as the ratio between flux error variances before and after inversion, with values ranging from 0% to 100%.

$$U_R = (1 - (C_f / C_{f0})) \times 100 \quad (3)$$

A value of 0 indicates no improvement of the initial prior errors, which corresponds to an absence of observation constraints in these pixels (emissions/fluxes informed purely by the prior).

2.2. Observation Network

This study utilizes the continuous measurement of CO₂ mole fractions from 6 towers in the Ile de France (a region located in the north-central part of France centered on the capital Paris) network. The tower locations are shown in Figure 1 and the exact coordinates of the towers, air intake's height and predominant wind direction are summarized in Table 1. The tower network was initiated with two towers equipped in late 2014 and increased gradually to seven towers by 2017. The towers are located along the dominant wind direction, similar to most mid-latitude cities, that is, from the South-West or the North-East sector 70% of the time. Data from 6 towers are only used in the inversion because the GHG sensor at of the sites Coubron went under maintenance during the study period.

The tower SAC, located 21 km from the urban area, is best suited to measure the background mixing ratios because of its upwind location and the absence of nearby sources. *Andilly* (AND) and *Gonesse* (GNS) are located in the northeastern part of the Ile de France region. AND is surrounded by a forested area with primary pollution from a waste processing facility located 1.4 km north of the tower. GNS is located 17 km North of Paris' center, in a residential area with noticeably large enhancements of CH₄ from a landfill and a waste treatment facility

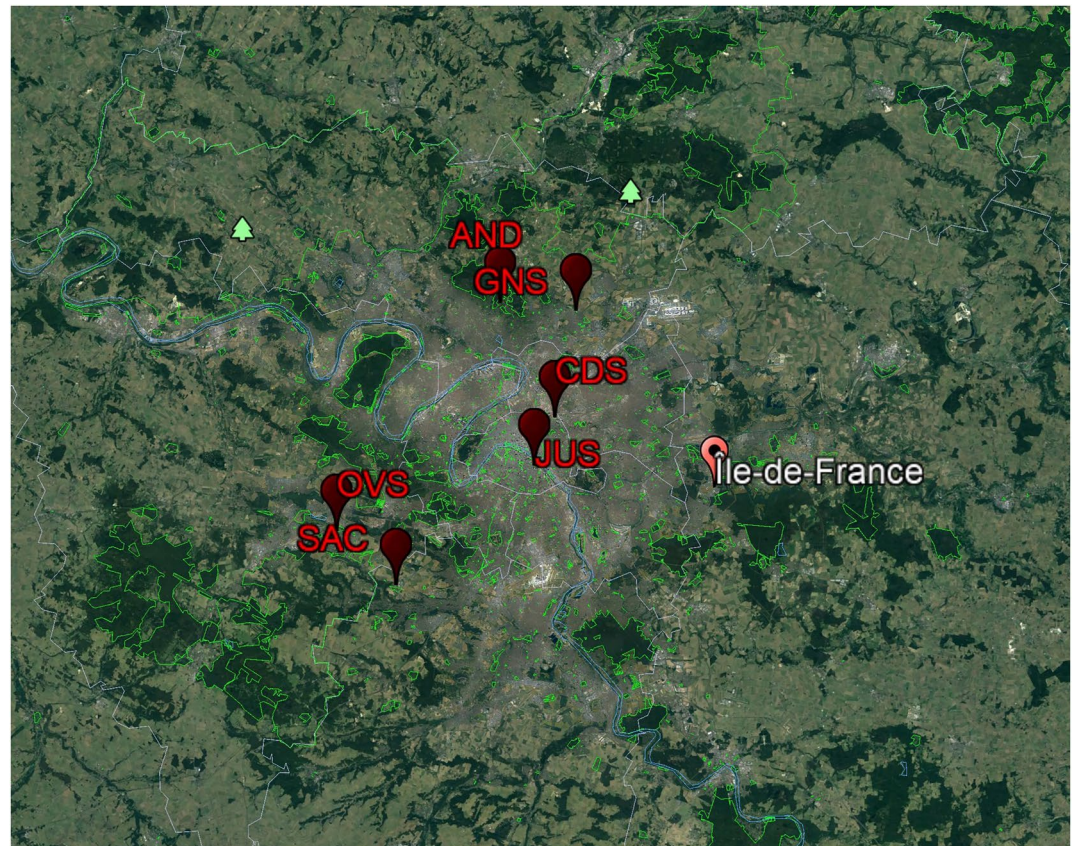


Figure 1. Location of the greenhouse gases measurement sites of the Ile de France network.

2.5 km north of the site. Two airports are located nearby: the international Paris airport Charles de Gaulle 8 km to the East, and the local Le Bourget airport 4.5 km in the south-east direction. *Jussieu (JUS)* and *Cité des Sciences (CDS)* are the two towers located at the core of the Paris urban area on building roofs. *JUS* is situated in the center of Paris, and *CDS* is located in the northeastern part of Paris city center. *Versailles-Saint-Quentin Observatory (OVS)* is located in the south-west part of the Ile de France region. *OVS* is 24 km south-west of Paris' center on the University roof, surrounded by a residential area. Possible pollution sources include Toussus-le-Noble airfield, 5 km South-East of the site.

Each site is equipped with a high precision Cavity RingDown Spectroscopy instrument (Picarro, inc.) to measure CO_2 , CH_4 , and CO mole fractions in dry air. The inlet of the instrument collects the air through a Synflex line with an outer diameter of $\frac{1}{4}$ inch. A $2 \mu\text{m}$ particulate filter is installed on the sampling line to protect the instrument's cavity. Except for *JUS* and *SAC*, all sites are using the same three cylinders to regularly (every 6 months) estimate

Table 1
Details of Sites in the Ile de France Network Used for Inversion

Tower (ID)	Location		Sea level altitude (m)	Air intake altitude (agl) (m)	Predominant wind direction
	Latitude ($^{\circ}\text{N}$)	Longitude ($^{\circ}\text{E}$)			
Andilly (AND)	49.0126	2.3018	175	60	South-west
Cité des Sciences (CDS)	48.8956	2.388	43	34	South
Gonesse (GNS)	49.0052	2.4205	81	36	South-east
Jussieu (JUS)	48.8464	2.35607	38	30	South-east
Versailles-Saint-Quentin Observatory (OVS)	48.7779	2.0486	150	20	South-east
Saclay (SAC)	48.7227	2.142	160	100	South, south-west

the instrument linearity. These cylinders are filled with synthetic air, and the mixing ratio of the species measured ranges from 371 to 504 ppm for CO₂, 1646–2082 ppb for CH₄, and 81–492 ppb for CO. For *JUS* we are using a dedicated set of three cylinders prepared in the same way. One additional calibration gas (called reference gas) is measured once a day to correct the measurements for short-term drift between two calibration sequences. All the cylinders used on the Ile de France network are calibrated at Laboratoire des Sciences du Climat et de l'environnement (LSCE), France before being installed at the sites. The calibration is performed with a reference instrument (Picarro G2401 - CO₂, CH₄, CO), calibrated against World Meteorological Organization-National Oceanic and Atmospheric Administration standards using six cylinders with mixing ratios varying from 368.75 to 516.57 ppm for CO₂, 1724.9–2548.9 ppb for CH₄, and 140.8–492.1 ppb for CO. The instrumentation differs slightly at *SAC*, which is labeled as Integrated Carbon Observation System (ICOS) station (Yver-Kwok et al., 2021). At this site, two instruments continuously measure CO₂, CH₄, and CO. Sampling lines are installed on the tower at three different heights: 15, 60, and 100 m above ground level. One of the instruments samples the air only from the 100 m line, while the other instrument samples from the three lines, hence switching sampling heights every 10 minutes. Monthly calibration is performed for the two analyzers using four gas cylinders with mixing ratios varying from 368 to 447 ppm for CO₂, 1700–2300 ppb for CH₄, and 67–1013 ppb for CO. The *SAC* data are processed every day by the ICOS processing chain, including the H₂O correction used to provide the mole fractions in dry air from the raw measurements done in wet air conditions and the calibration correction using a linear fit from the four reference cylinders (Hazan et al., 2016). A similar scheme is used for the other stations, the only exception being the use of the additional reference, as explained before. In order to control the repeatability of the measurements, a quality control gas is systematically measured once a day in each station. The CO₂ mole fractions of those target-gas are assigned at the LSCE, with a calibration using the World Meteorological Organization reference scale. Overall, the mean values of the target tanks measured at the 6 stations differ from the assigned values by ± 0.07 ppm. The standard deviations of the daily injections are lower or equal to 0.02 ppm at all the stations, with extreme differences to the assigned values ranging between +0.11 and –0.13 ppm. Those values do not account for the uncertainties of dry gas. According to Rella et al. (2013), the uncertainty associated with the water vapor correction is lower than 0.1 ppm for H₂O concentrations below 2%, which represent 98% of the data set considered in our study. The uncertainty is reduced to ± 0.05 ppm using correction factors established at LSCE for each instrument (Laurent et al., 2019).

2.3. Lagrangian Model and Source Receptor Matrix

In our Bayesian formulation, the atmospheric transport operator relates surface fluxes to atmospheric mixing ratios. The Jacobian matrix H used to represent it in the inversion was generated using backward simulations of the Lagrangian Particle Dispersion Model (LPDM) described by Uliasz (1994). In forward mode, particles are released at the source locations and tracked until they pass through the receptor (observation tower). However, when the number of sources is larger than the number of receptors, running an LPDM in backward mode becomes more computationally efficient. Mass-free particles are released at each receptor location and sampled backward in time to potential source regions (Seibert & Frank, 2004). The LPDM was evaluated and used in several other inverse studies over different regions (e.g., Karion et al., 2015; Lauvaux et al., 2008).

LPDM is driven by the hourly three-dimensional fields of mean winds (u , v , w), potential temperature, and turbulent kinetic energy obtained from the WRF model (Skamarock et al., 2008) with a chemistry module. WRF-Chem v3.9.1 was configured with one-way nesting of the modeling domain at a horizontal grid resolution of 1 km that covers the Ile de France region and its surroundings (Lian et al., 2021). The model domain has 44 vertical layers extending from the surface to 100 hPa wherein 25 layers are arranged below 1.5 km and the height of the first layer top is approximately 3.1 m above the ground level (Lian et al., 2021). Observations from surface weather station data and upper-air meteorological fields from the Research Data Archive at the National Center for Atmospheric Research were also assimilated to WRF-Chem (Lian et al., 2019). Initial and boundary conditions for the WRF-Chem were obtained from the global European Center for Medium-Range Weather Forecasts (ECMWF) Re-Analysis data (ERA5) with $0.75^\circ \times 0.75^\circ$ horizontal resolution (Berrisford et al., 2009). The atmospheric boundary layer scheme used is the Mellor-Yamada-Janjic (MYJ) scheme (Janjić, 1990, 1994) coupled with the Monin-Obukhov (Jancic Eta) scheme to represent the atmospheric surface layer (Janjic, 1996). Urban canopy model BEP (Building Effect Parameterization) (Martilli et al., 2002) is used as urban parameterization, and the NOAH land surface model (Chen and Dudhia, 2001) was used to simulate the surface energy balance over non-urban land. A more detailed description of the model parameterization can be found in Lian et al. (2018, 2021).

In addition to the meteorological fields, we also used the CO₂ biogenic fluxes from the WRF-Chem simulation estimated using the Vegetation Photosynthesis and Respiration Model (VPRM) (Ahmadov et al., 2007, 2009; Mahadevan et al., 2008) which was coupled online to the WRF-Chem model.

Over an hour, 2,700 particles were released incrementally every 20 s from each measurement tower in the Ile-de-France network and traced backward-in-time for 24 hr. Most particles have left the simulation domain after 10 hr, except during extremely low wind conditions. The maximum travel time of particles based on the 95th percentile was 8 hr with a mean of 4 hr. As air masses transport particles, their locations are stored every two minutes for any particle located near the surface (within the surface layer, ~50 m) and finally aggregated over a fixed time interval of 1 hr. This spatial information is used to generate the surface footprint of each tower observation (or influence function). The model calculated particle counts t_{count} as

$$t_{count} = r_{part} \times (3600/r_{dt}) \times (60/out_{dt}) \quad (4)$$

where r_{part} is the number of particles released at every model time step (2,700), r_{dt} is the model time step in seconds (20) and out_{dt} is the time interval between two output files in minutes (2). From the particle count obtained here, we generate the influence function, defined as $g2ppm$ as follows:

$$g2ppm = (count/t_{count}) \times (g/(1000 \times \Delta P)) \times ((29 \times 10^6)/44) \quad (5)$$

where $count$ is the number of particles in the grid cells, ΔP is the pressure difference in the surface layer (~720 Pa), and g is Earth's gravity.

The surface layer height was set to 50 m which corresponds to approximately 720 Pa. In a well-mixed condition, the source–receptor relationship should be independent of the surface layer thickness, as long as the layer is not too deep, as the particle count will be adjusted proportionally to the grid box volume (Seibert & Frank, 2004). The spatial resolution of the gridded domain consisting of 90 × 90 grid boxes was set to be 1 × 1 km. The surface fluxes represented in g CO₂ km² hr⁻¹ are projected using H into mixing ratios at the measurement sites in units of ppm.

2.4. Prior Flux Estimates and Error Covariance Matrix

2.4.1. Fossil Fuel Emission Inventory

In our study, a high-resolution inventory of anthropogenic CO₂ emissions (Origins. Earth (<https://www.origins.earth>)) developed over the Ile-de-France region was used for the inversion. The data set includes the emissions from six sectors: Industry (including cement), transport, tertiary emissions, residential, energy and waste.

The gridded emissions are based on regional totals downscaled to a 1 × 1 km resolution using spatial proxies (i.e., high-resolution French population census, coordination of information on the environment land-use cover, locations of the thermal power stations, incinerators, and main emitting industries) at 1h time resolution. For stationary combustion, the 85 point-sources corresponding to industries, power plants and waste burning have been identified; paid employment density is used as a proxy to spatialize the remaining economic emissions. Building age, usage, and type are used as a proxy for the spatial distribution of residential and tertiary emissions. Local energy consumption rates are combined for temporal distributions. For road transport, spatial and temporal distributions are based on the traffic activity measured by a network of 3,345 traffic flow sensors deployed across Paris. More details about the inventory are described in Lian et al. (2022, Appendix, text S1). Over the Paris metropolitan area, the commercial and residential sectors (buildings) combined contribute to almost 58% of the total CO₂ emissions, 22% is attributed to on-road transport, and the remaining 20% is distributed among the other sectors.

In the second part of the study, CO:CO₂ ratios were used to optimize emissions from *traffic* and *nontraffic* sectors referred to as *others* in the present study. Gridded CO/CO₂ ratios were obtained from TNO GHG and co-emitted species database (GHGco) at a resolution of 0.1° × 0.05° (~6 × 6 km) (van der Gon, 2019). TNO gives emission ratios for public power, industry, other stationary combustion, fugitives, solvents, road transport, shipping, aviation, off-road transport, waste and agriculture sectors. The data set covers the entire European domain for the GHGs/CO₂ (distinguishing between fossil fuel and biofuel CO₂), methane, and key co-emitted species that may be used as tracers: CO (also distinguishing between fossil and biofuel) and nitrogen oxides. The emission

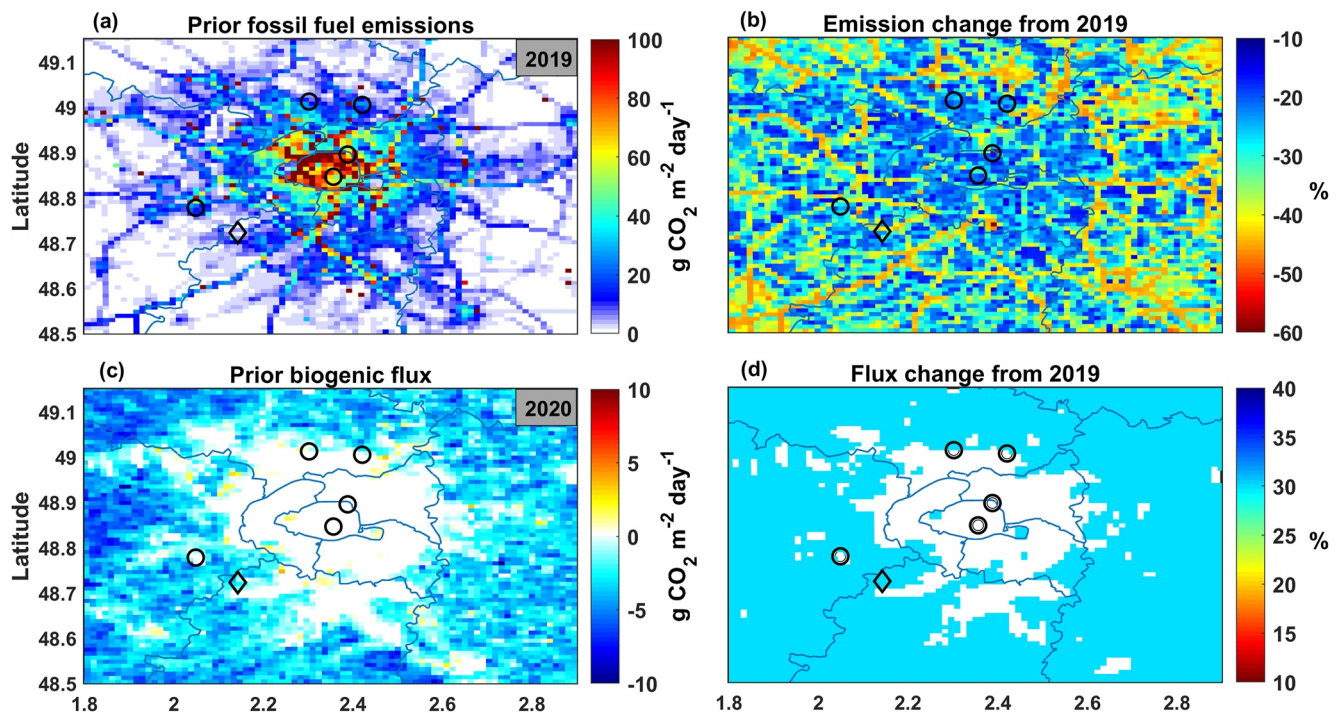


Figure 2. Prior flux maps for the fossil fuel emission and biogenic fluxes (daytime + nighttime) from the Origins.Earth inventory. The top row is the CO₂ emissions during 2019 spring and percentage emission changes in 2020 compared to 2019. The bottom row shows the same for biogenic fluxes.

datasets were developed primarily based on the reported data. Gaps in the reported data were filled using other emission data from the GHG and air pollution interactions and synergies (GAINS) model (van der Gon, 2019). Thereafter, a consistent spatial distribution methodology is applied for Europe where each emission source gets a specific proxy assigned, which defined the way emissions are to be spatially distributed over the country. For point sources, information was collected on the location of power plants, large industrial installations, oil and gas production sites, airports and waste treatment locations (e.g., landfills). For area sources, proxies are collected that are thought to best represent the spatial variability of each specific emission source (van der Gon, 2019). More details about the inventory are described in van der Gon. (2019).

2.4.2. Biogenic Flux

Biogenic CO₂ fluxes are generated using the VPRM model initiated with meteorological fields from WRF-Chem. This simple model uses meteorological, remote sensing, and tower flux data to represent surface fluxes (Mahadevan et al., 2008). VPRM uses downward shortwave radiation, surface temperatures, and vegetation indices derived from the 8-D Moderate Resolution Imaging Spectrometer (MODIS) Surface Reflectance Product (MOD09A1). For each vegetation category, four parameters (PAR0, λ, α, β) are optimized against eddy covariance flux measurements over Europe collected during the Integrated EU project “CarboEurope-IP” (<http://www.carboeurope.org/>, last access: 12 November 2019). VPRM uses land cover data derived from the 1 km global Synergetic Land Cover Product (SYNMAP; Jung et al., 2006; Ahmadov et al., 2007, 2009) classified into eight different vegetation classes. The eddy covariance data upon which VPRM has been calibrated do not necessarily represent the vegetation of the Paris area, which is a source of uncertainty in modeled biogenic CO₂ fluxes.

Figure 2 shows the total fossil fuel CO₂ emissions from Origins.Earth and biogenic fluxes from VPRM for the 2019 spring months (March–May) and the relative changes (percentage) in the emissions and fluxes in 2020 compared to 2019. Fossil fuel emissions are high in the central and north-west Paris region (~90 g CO₂ m⁻² day⁻¹) and gradually decrease away from the central Paris region. In addition, a few hotspots are scattered throughout the domain. These include 85 individually identified hotspots representing 8.07 Mt CO₂ in 2018 over 34.80 MtCO₂. In 2020, the high-resolution inventory suggests that the net emissions decreased by about 10%–60% (30 ± 5 MtCO₂), most probably due to the pandemic lockdown (two strict confinements in France lasting several months) (Figure 2b). The biogenic fluxes shown in Figure 2c represent the Net Ecosystem Exchange (NEE) with

a negative sign indicating net CO₂ uptake. The modeled NEE values are negative over most of the domain (with uptake of up to 10 g CO₂ m⁻² day⁻¹), except over the central Paris region where the values are equal or close to 0, which comes from the SYNMAP land use in VPRM. NEE show a uniform 30% increase in 2020 without any spatial variations compared to 2019, as suggested by the MODIS driver data and annual meteorological conditions.

2.4.3. Prior Emission Errors

The high spatial and temporal resolutions of the Origins.Earth emission fields are not associated with an explicit calculation of their associated errors. According to the Intergovernmental Panel on Climate Change (IPCC) guidelines, fossil fuel emission uncertainty includes “naturally” occurring variability in the emissions at the annual/national scale. At high resolutions, emissions uncertainties are due to errors in emission factors, missing input data, and temporal/spatial downscaling (Oda et al., 2018). In a study by Lauvaux et al. (2016), error variances were represented as a percentage of net emissions because of the unavailability of a better solution. Here, sector-based emissions errors are defined as 100% of the emissions at 1 km resolution, corresponding to a total prior uncertainty of about 40% once aggregated over the domain. According to IPCC, quantitative uncertainty analysis is performed by estimating the 95% confidence interval of the emissions and sink estimates for individual categories and the total inventory. In the case of global emissions, the uncertainty can range from as low as 8% to more than 50% (Eggleston et al., 2006). However, the uncertainty for different sectors can range from 2% to 8% on the national scale, whereas the total uncertainty of inventory usually adds up to 5%–20% (Eggleston et al., 2006).

With a Bayesian inversion using linear scaling factors, the inverse solutions can become negative. However, the scaling of the error variances to the prior emissions over 5 days limits the occurrence of negative solutions to very few isolated cases (Lauvaux et al., 2016). It also implies that pixels with low emissions (=low uncertainties) are too constrained to allow large corrections. For that specific reason, our high-resolution inventory takes the location of 85 main emission industries and declared CO₂ emissions from them as “unknown”, which would inevitably not be determined by our approach. The inversion has been tested for two spatial correlation lengths, that is, $L = 4$ km and $L = 20$ km for the emissions errors. Temporal correlations are considered to be negligible in our study, assuming that temporal correlations have vanished beyond 5 days because consecutive 5-days include “weekdays only” and a combination of weekdays and weekends. A test study has been carried out to analyze the sensitivity of the inversion to the prior emission errors where prior emissions errors are defined as 60% of the net emissions. It would represent a total error of 25% over the domain for 3 months (March–May), including spatial error correlations. Dependence of error variances on the correlation length is defined similarly to Lauvaux et al. (2012) where exponentially decaying correlations with the distance have been applied among urban pixels only (based on the National land cover database 2010). The distance-based correlation matrix (m_L) is created first and then combined with each land cover type assuming no correlation between urban and nonurban pixels m_{urb} . The combined matrix (M) is created assuming equal weights from both the correlation matrices using the following equation (Lauvaux et al., 2016).

$$M = \sqrt{m_L} \times \sqrt{m_{urb}} \quad (6)$$

The 5-day inversion window was defined based on the length of synoptic and mesoscale events. For a shorter inversion time window (e.g., daily), the surface coverage of aggregated tower footprints would be spatially-limited. However, short-term variations may be misrepresented by our solution. Here, we focused on 5-day mean emission estimates to constrain the spatial distribution over the whole area, assuming the prior diurnal variations are correct (similar to Lauvaux et al., 2016). The inversion is carried out over 5-day inversion windows over three months (March–May) of 2019 and 2020.

2.4.4. Balance of Error Contributions

In our study, errors in the WRF-Chem modeling system are propagated into the inversion system by estimating the error variances based on metrics representing the model meteorological performances. First, error variances are scaled using the normalized distance of a X^2 distribution to compute the average variance for a 5-day period. Second, using the WRF-Chem generated wind speed and direction, variances are adjusted for each hour. Furthermore, the first step is repeated for the adjusted variances to ensure the error balance within the inversion system. More details about this approach are described in Lauvaux et al. (2016). Observation errors are considered

uncorrelated in both time and space. Whereas day-to-day correlations might be weak and hourly correlations might occur within a single afternoon. However, in the absence of rigorous quantification, we assumed that hourly correlations are negligible. Therefore, the observation correlation length is set as 0. Our variance estimation approach helps to remove singular time steps associated with poor transport model performances (Lauvaux et al., 2016). The ability of the WRF-Chem model to predict the wind direction and speed (in terms of Mean Absolute Errors (MAE)) has been quantified using the observed counterparts (Lian et al., 2018). Hourly MAE over the inversion domain was determined for both wind direction and speed, a proxy for transport errors over the entire domain (at all of our sites) at a given hour. Deviations of the model predictions from the observations point to the performance of the WRF-Chem model.

The variances in the inversion represent the errors in the meteorological parameters that cannot be predicted by the model, along with prior flux and transport errors. A χ^2 normalized distance λ is defined as,

$$\lambda = 1/n \left[(y - Hf_0)^T (HC_{f_0}H^T + C_c)^{-1} (y - Hf_0) \right] \quad (7)$$

which informs about the balance between the prior error and the observation error in the inversion (Kaminski et al., 2001).

2.4.5. Boundary Inflow

In a domain-limited inversion, the flux estimation depends on the contribution from the background signals that originated outside the domain and were transported to the observation sites (Goekede et al., 2010). Accounting for the airflow through the boundaries makes a noticeable difference in quantifying the amount of CO₂ from distant sources/sinks compared to local emissions (Lauvaux et al., 2012). This quantity can be estimated by using measurements upwind of the area, which represents, for the most part, the influence of remote fluxes over the region of interest. However, the measured upwind mixing ratios are also influenced by local fluxes and local dynamics, hence less representative of the domain background. Since the air inflow depends on the direction of the wind and its variability, the selection of the upwind site will vary in time.

There are three primary methods to select the best-suited background mixing ratios: (1) deriving the background directly from all the observations, for example, by taking the minimum mixing ratio over the period; (2) using hourly mixing ratios from a specific site; and (3) selecting mixing ratios from upwind sites based on wind direction. The first method has been utilized in many halocarbon studies (e.g., Brunner et al., 2017; Hu et al., 2016; Manning et al., 2003). The second approach is ideal when only one site is located outside the city limits. In the present study, we have tested only methods 2 and 3 to derive background mixing ratios for the inversion. Method 1 has not been tested here because based on a study by Lauvaux et al. (2016), it introduced a positive bias in the inverse solution by artificially increasing the emissions over the city. In addition, this method is the least realistic because the lowest concentrations are often observed at the end of the day, which is inconsistent with the advection time of air masses across the city (Lauvaux et al., 2016). In method 2, hourly mixing ratios from SAC tower for 12–17 UTC are used as the background. The site is upwind most of the time, and it covers a larger footprint that does not include major sources and vegetation cover. This is a simple method used for the inversion using a limited number of towers. In method 3, we selected *AND* or *SAC* as background sites, depending on wind direction. When the wind is between 135° and 315°, *SAC* is used as the background site, whereas if the wind is >315° and <135°, *AND* is used as the background site. In both the cases, the local influence is then subtracted from the observed values based on the modeled influence of prior emissions and biogenic fluxes originating from our inversion domain, similar to Lauvaux et al. (2020).

2.5. Inversion With an Additional Tracer CO

The second part of the study aims to delineate traffic CO₂ emissions using CO mixing ratios and CO:CO₂ ratio in addition to CO₂. Figure 3 shows the total CO₂ emissions (March-May) from the Origins.Earth inventory for two different sectors for 2019 and their respective changes in 2020. Here, the fossil fuel emissions are grouped into *traffic* and *others* (*nontraffic*) emissions. The *traffic* sector is comprised of on-road and off-road transport emissions, whereas *others* emissions cover industrial, public power sector, stationary combustion (power plants, combined heat and power production plants, industrial combustion plants, and district heating plants, as well as small plants, e.g., stoves and residential boilers), and emissions from waste, solvents, and agriculture. In 2019,

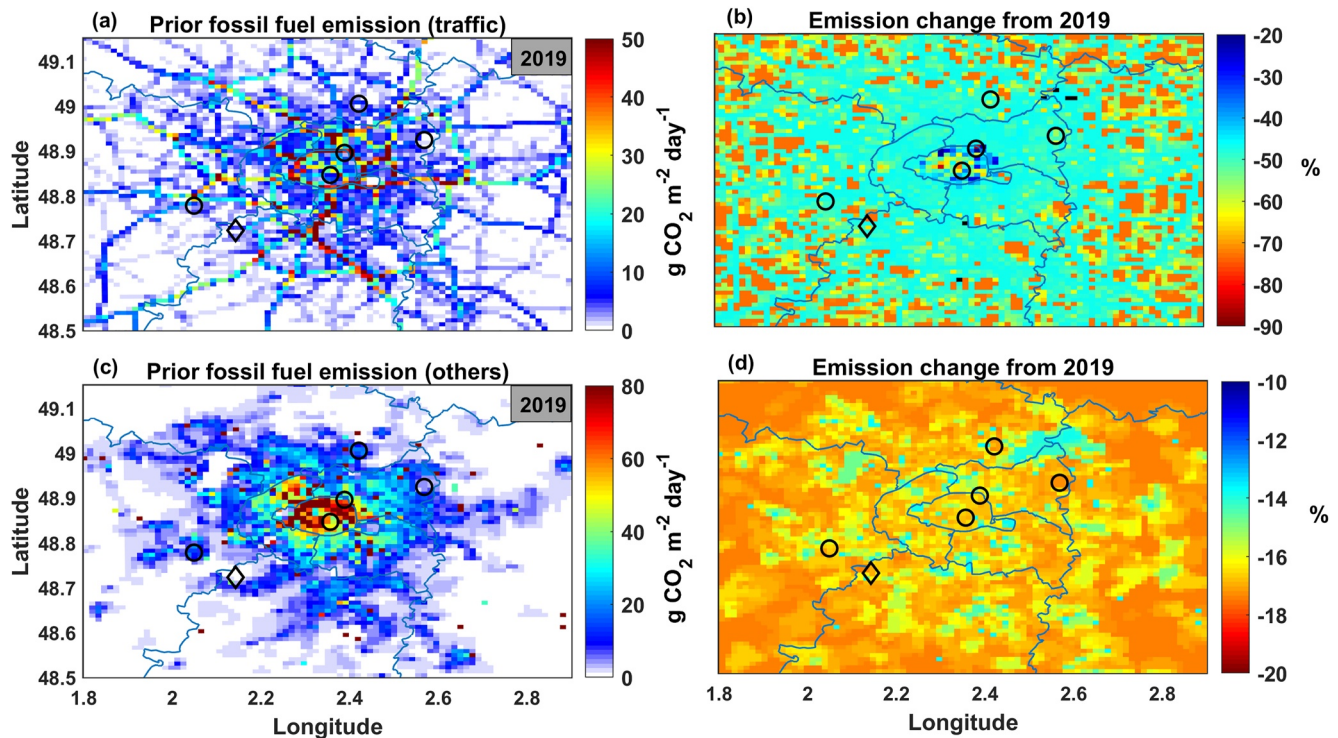


Figure 3. Prior flux maps for the two fossil fuel emission sectors. CO₂ emissions in 2019 from (a) *traffic* and (c) *other* sources (industry, stationary and residential) and their respective emission changes in 2020 compared to 2019 for (b) *traffic* and (d) *other* sources.

traffic emissions are mainly concentrated around the Paris city and south of the city administrative boundaries. Emissions from *Others* sector is large in the central Paris region where most of the industries are located. In 2020, both the sectors showed a negative change indicating the emission reduction by about 20% for *traffic* and 14%–16% for *others* sector. Reduction in *traffic* emission is more prominent in the central Paris region compared to the boundaries. This explains the emission reduction during the shutdown of the city during the COVID 19 lockdown.

In our joint CO-CO₂ inversion, mean CO:CO₂ ratios were calculated from the gridded ratios based on the TNO inventory for all sectors and utilized along with the hourly CO emissions. These mean sectoral factors are multiplied by the gridded prior emissions and aggregated into *traffic* and *others* sectors to obtain gridded CO emissions, similar to Nathan et al. (2018) and Lauvaux et al. (2020).

3. Results

3.1. Inversion With CO₂ Data

3.1.1. Spatial Distribution of Posterior Fluxes

Figure 4 shows the spatial distributions of total CO₂ fossil fuel emission (March–May) differences from prior for 2019 and 2020 (left column) and their respective percentage error reductions (right column). In 2019, fossil fuel emissions significantly increased from prior over the central Paris region (about 66% (Figure 2)). On the outskirts of the city, the increase is only <50 g CO₂ m⁻² day⁻¹, down to zero outside Paris in the vicinity of the suburban towers (*AND*, *GNS*, and *OVS*). In 2020, the rate of increase in the emissions after inversion is small compared to 2019 indicating the effect of lockdown where most of the sources were shut down. A recent study by Lian et al. (2022) reported that the decrease in the magnitude is associated with a reduction in traffic emissions as well as milder temperature than normal, which has an influence on household emissions.

Figures 4b and 4d depict the gridded percentage error reductions after inversion for 2019 and 2020. The inversion reduces the uncertainty in the emissions in the range of 2%–10%. The area surrounding the *CDS* and *JUS* sites

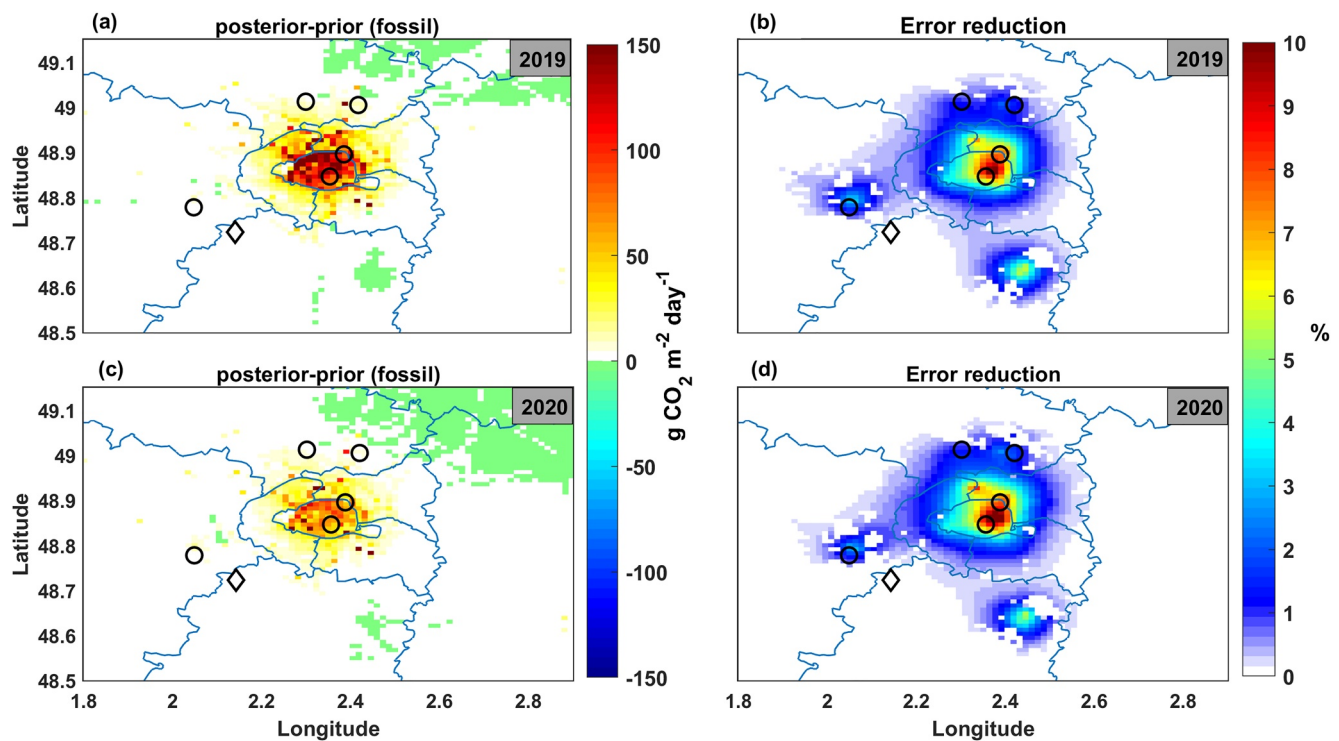


Figure 4. Total fossil fuel emission change for (a) 2019 and (c) 2020, and their corresponding percentage error reductions (b and d). The five measurement sites from which CO₂ mixing ratios are assimilated are marked as black circles and the background SAC tower is marked as a diamond shape. The prior emissions used here are from the respective years.

shows the maximum error reduction, indicating that both sites provide a significant atmospheric constraint on the fossil fuel emissions in downtown Paris whereas the rest of the urban area shows smaller reductions below 5%. In contrast, the emission change and error reduction are close to zero outside the metropolitan area, a direct consequence of the absence of fossil fuel sources outside the city limits in the Origins.Earth inventory.

Figure 5 shows the changes in biogenic fluxes after inversion and their corresponding percentage error reductions for 2019 and 2020. Compared to fossil fuel emissions, the magnitude of biogenic fluxes is about three orders of magnitude less. In the vicinity of *AND*, *GNS*, and *OVS* towers, the biogenic fluxes are increased compared to the rest of the domain. The absence of biogenic fluxes in the central Paris region (Figure 2) indicates that the VPRM simulations exclude small parks and gardens in this area. Land cover maps would be needed at higher resolutions, but the current configuration only considers MODIS data at 250-m resolution. In addition, the measurement sites that are used in the inversion are mostly sensitive to fossil fuel emissions in their vicinity. Error reductions in Figures 5b and 5d for biogenic CO₂ fluxes show no change in most parts of the domain except small reductions of about 0.2% around the suburban towers.

3.1.2. Flux Time Series

The evolution of emissions throughout the inversion time-period is analyzed based on time series from March to May of each year. Emissions are summed spatially and temporally (i.e., a combination of optimized day-time emissions and inventory-based night-time emissions) to represent the total 5-day fossil fuel emissions as shown in Figure 6. Shaded areas around the emission lines represent their respective uncertainties.

Fossil fuel CO₂ emissions increased significantly after inversion in 2019 over the entire period. The increase was largest (about 0.6 MtCO₂) at the start of March, which gradually reduced to 0.3 MtCO₂ difference in the last week of April. It is also noticeable that fluctuations in the posterior emissions are larger than the prior. In 2020, fossil fuel emissions were large (1.1 MtCO₂) in the first half of March similar to 2019, which was subsequently reduced to 0.5 MtCO₂ at the beginning of the lockdown period. Here, the decrease in emissions was much faster compared to 2019. The posterior emissions in the lockdown window have become almost close to the prior

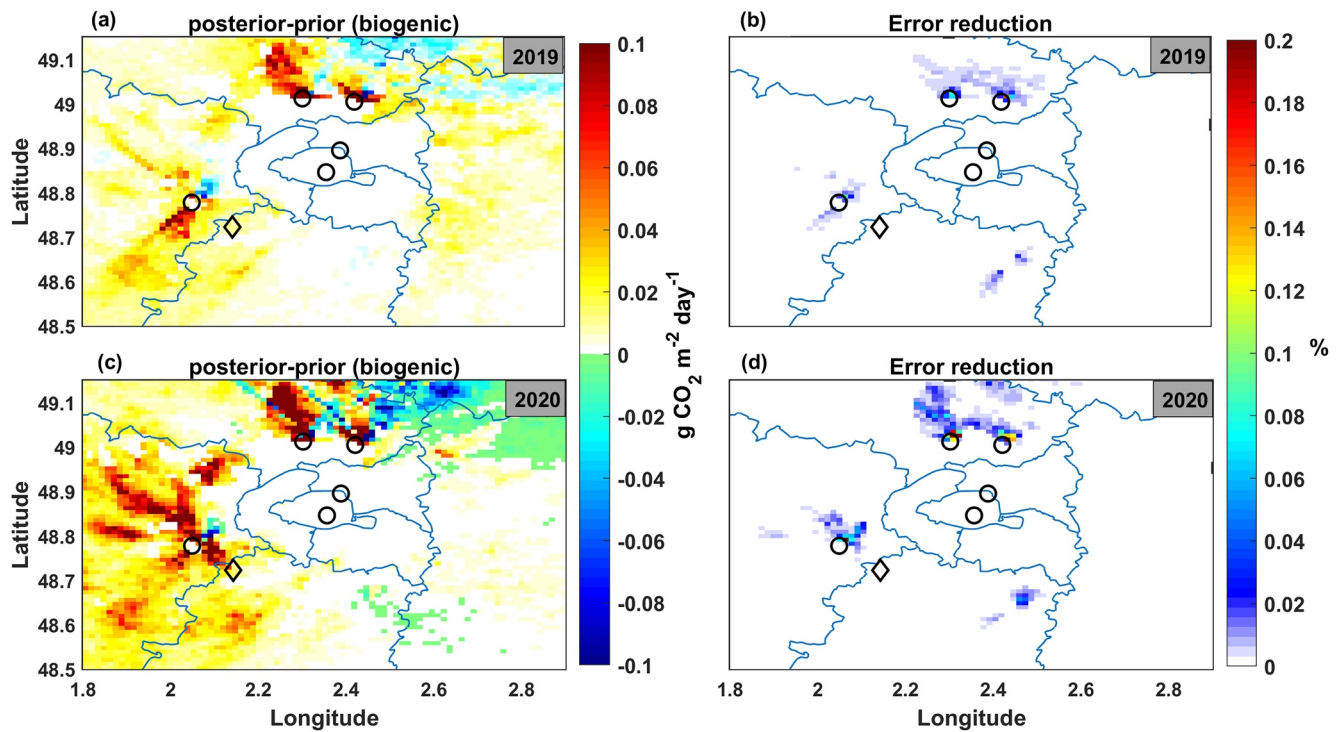


Figure 5. Total biogenic flux change for (a) 2019 and (c) 2020, and their corresponding percentage error reductions (b and d). The five measurement sites from which CO_2 mixing ratios are assimilated are marked as black circles and the background SAC tower is marked as a diamond shape.

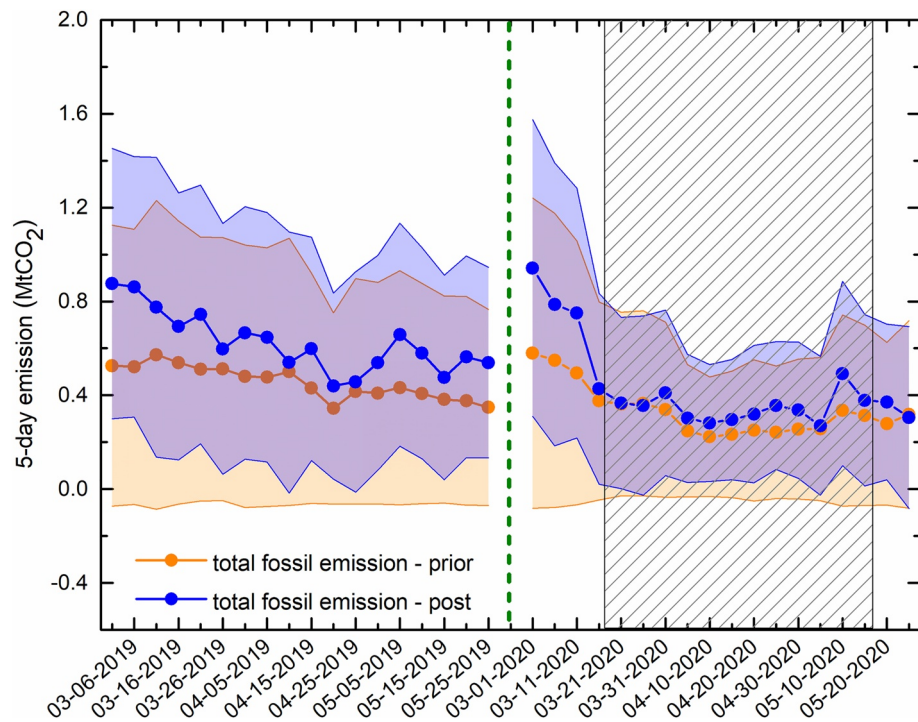


Figure 6. Five-day time series of prior and posterior fossil fuel emissions (day + nighttime) and their respective uncertainties for 2019 and 2020 (colored shaded area). The COVID 19 confinement period in 2020 is shown as shaded gray zones.

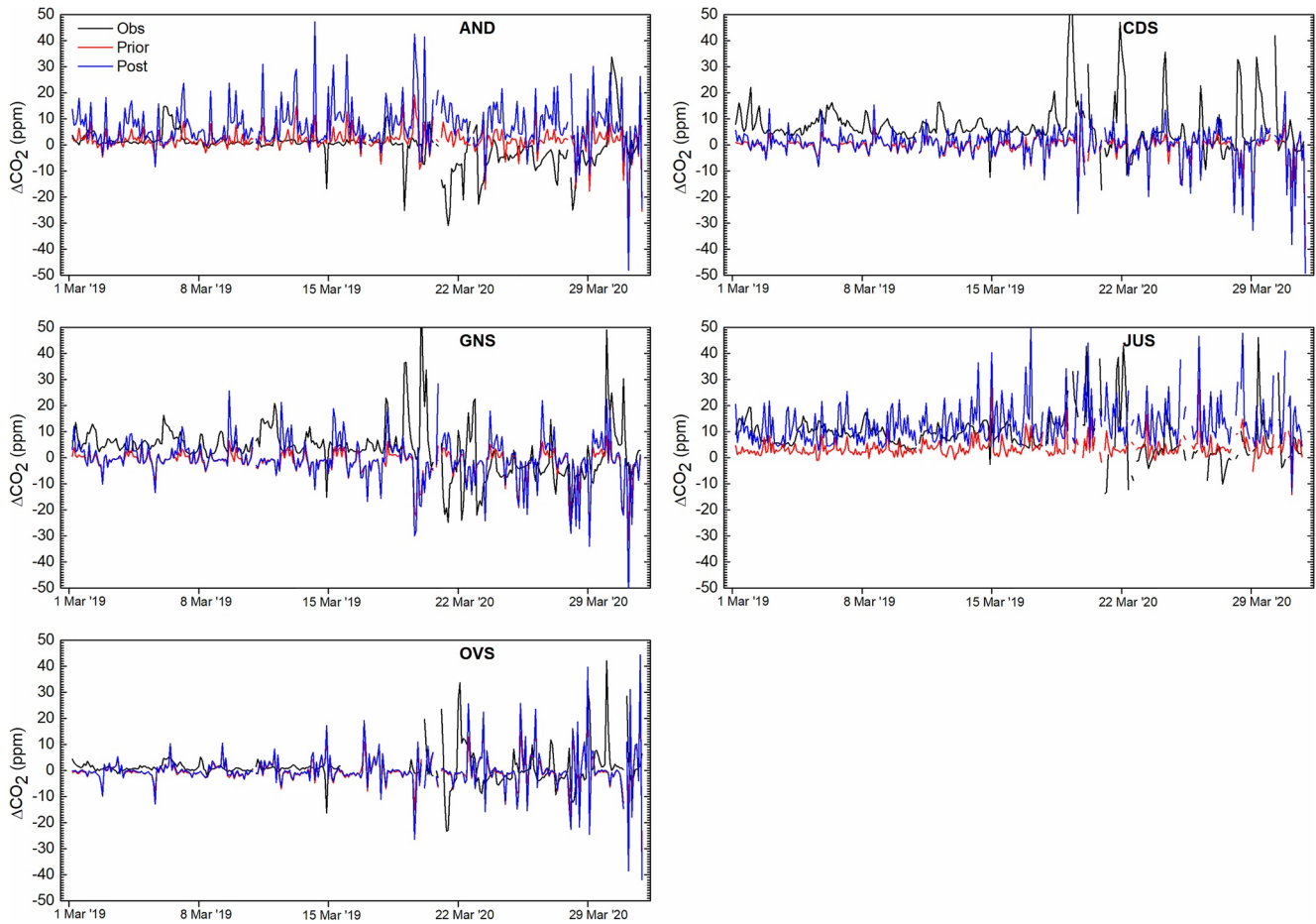


Figure 7. CO₂ atmospheric mixing ratios (difference from the background) from WRF-LPDM footprints coupled to the Origins.Earth prior emissions (in red), to the posterior emissions (in blue), and the observations (black) for the five surface towers for March 2019.

emissions indicating that the Origins.Earth inventory well represented the emission reduction during this period. The large reduction after the initial weeks of March 2020 is coincidental with the COVID 19 lockdown period. Our inversion system only constrains emissions during day-time (7–17 UTC), but we expect little to no change at night except external environmental factors (e.g., temperature).

3.1.3. Posterior Mixing Ratios—Measuring the Impact of Inversion

Our inversion system was designed to minimize the mismatches between observed and modeled mixing ratios. However, the presence of spikes and the high variability in observations motivates an examination of the posterior model-data mixing ratio mismatches to evaluate the ability of our inversion system to simulate the local variations. We note here that the posterior mixing ratio gradients are not shown, but the change from the background represents the impact of local sources and sinks. Prior and posterior mixing ratio changes were determined in two steps: (1) we multiplied hourly footprints of each site (including background SAC) with the 5-day averaged fluxes (fossil + biogenic) for the day-time (7–17 UTC), and (2) removed the corresponding mixing ratios at SAC from the other towers (hence excluding the local influence similar to the inversion).

Figure 7 shows the hourly mixing ratio difference from the background station for the five towers used in the inversion (excluding SAC) for March 2019. All the tower observations show large fluctuations because of the local influence and have larger magnitudes compared to the modeled values. Inversion resulted in a positive readjustment of emissions and the same is reflected in the mixing ratios as well. However, there is a few exceptions are seen; for example, *CDS* shows negative posterior mixing ratios despite its location in the city center whereas *JUS* shows large positive mixing ratios after inversion. We expect that *CDS* does not capture all the emissions during this period from Paris city because of unfavorable wind conditions. Another exception is seen for *AND*,

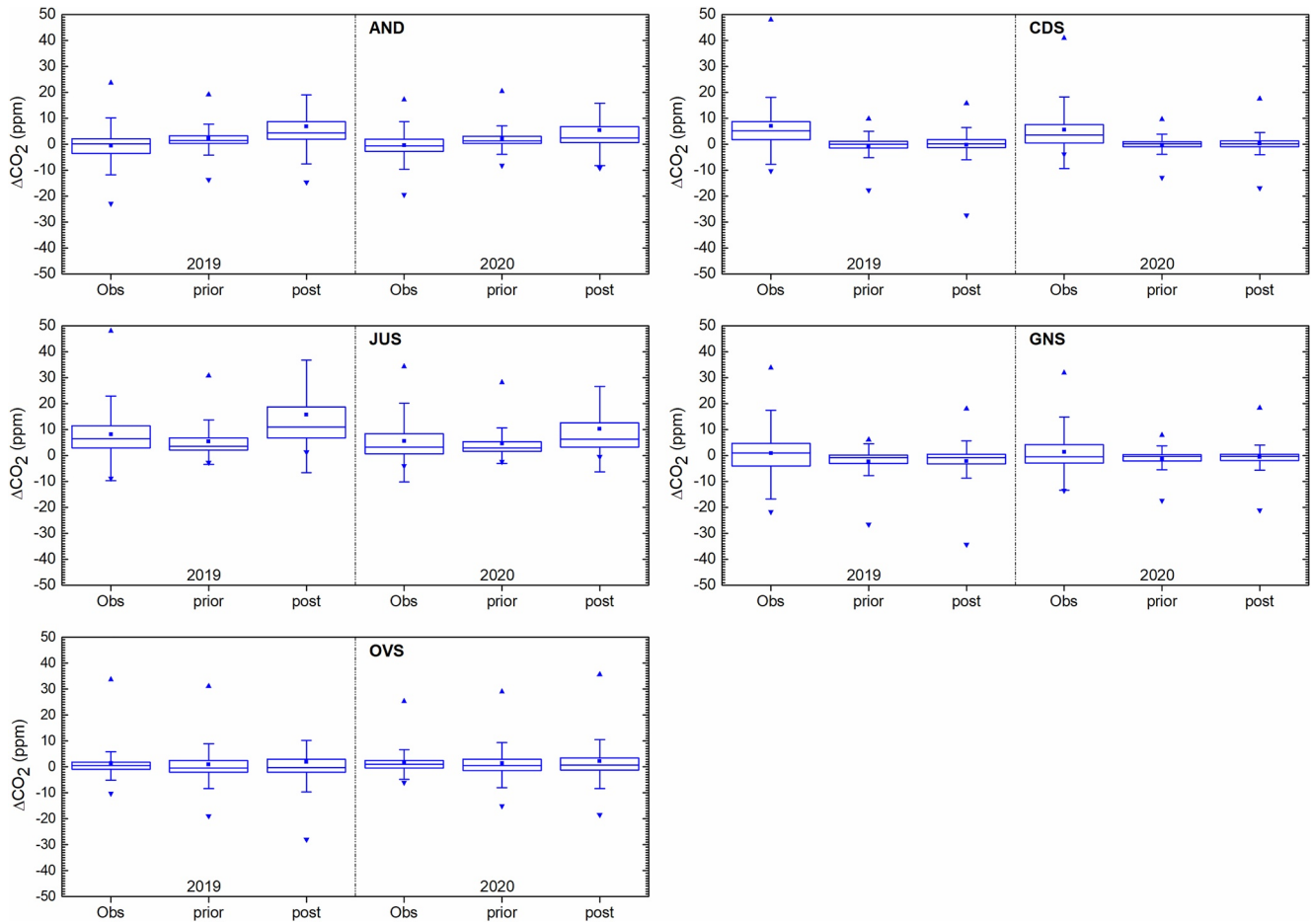


Figure 8. Quartiles of the hourly mixing ratios (difference from background) (for the individual observation towers for 2019 and 2020).

where the posterior mixing ratios show larger values despite its location outside city limits. for *GNS* and *OVS*, the prior mixing ratios were having very low magnitude, which is enhanced after the inversion.

Figure 8 shows the quartiles of hourly observations, prior and posterior mixing ratios of the five towers used in the inversion for the periods March-May of 2019 and 2020. The mixing ratio threshold was set to 50 ppm to remove outliers, which was around less than 5% of the total number. Corrections in the prior fluxes vary between each tower with a maximum for *JUS* where the initial mismatch between prior and observations is reduced from 7 to 3 ppm (median) after inversion. *CDS*, *GNS* and *OVS* show a very small correction of about 1 ppm whereas mismatch has been amplified for *AND*. A similar pattern is seen for 2020 where the average mixing ratios fall into a very small range except for *AND*.

3.2. Inversion With an Additional Tracer CO

3.2.1. CO-CO₂ Inversion—Spatial Distribution of Sectoral Emissions

Here, we aim to optimize fossil fuel CO₂ emissions separately for the *traffic* and *nontraffic (others)* sectors using CO and CO₂ mole fractions. Figure 9 shows the maps of emission difference from the prior for the *traffic* sector and respective percentage error reductions (right column) for 2019 and 2020. In 2019, our inversion system shows an increase in the *traffic* emissions by about 16% (20–30 g CO₂ m⁻² day⁻¹) within the Paris metropolitan area compared to only 9% (<10 g CO₂ m⁻² day⁻¹) in 2020 over the same area. The area surrounding the towers in the north-east and south-west quadrants shows little to no change in emissions. The positive readjustment of emissions in 2019 and 2020 leads to the impression that the prior emissions were underestimated. Compared to 2019, the posterior *traffic* emissions reduced by about 70% in 2020. Error reductions in Figures 9b and 9d show

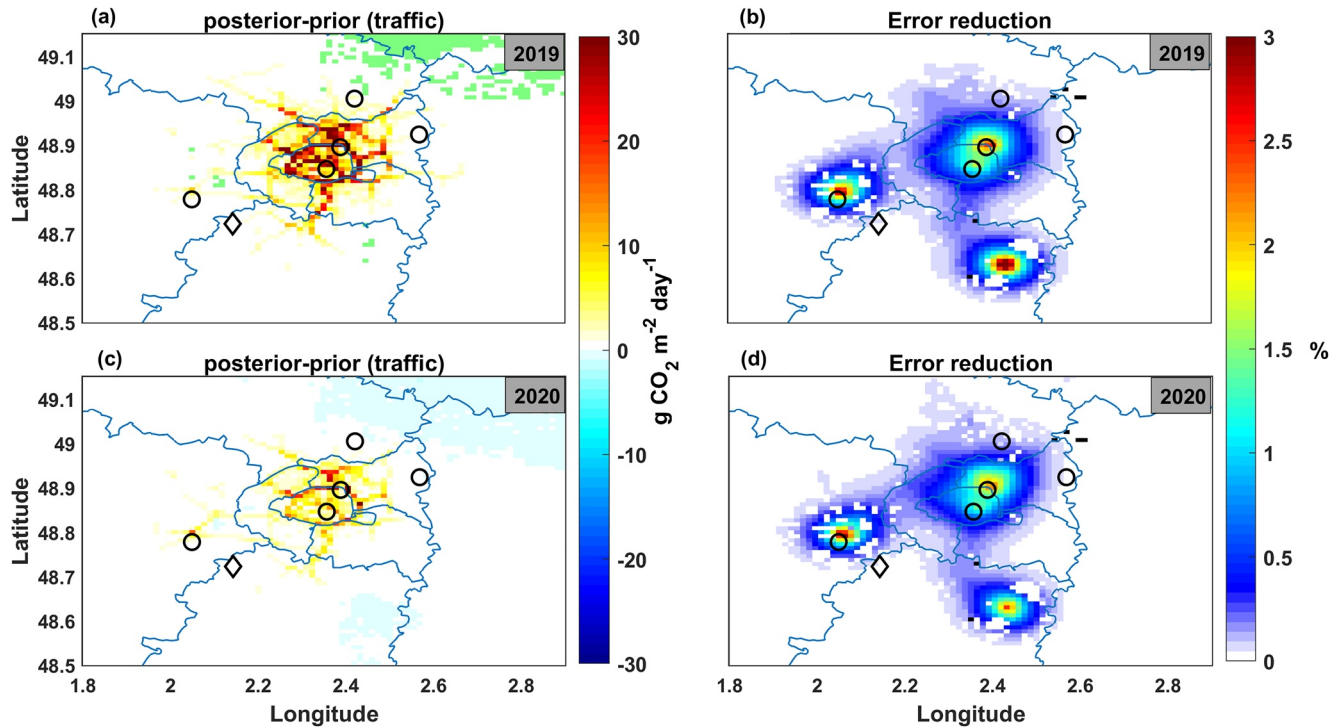


Figure 9. Flux maps of change in emission (day + nighttime) from prior after inversion for the *traffic* sector for (a) 2019 and (c) 2020 and their corresponding percentage error reductions (b and d). Towers used for the inversion are marked as circles and diamond shape.

a similar pattern for 2019 and 2020, with larger reductions in 2020. The error reduction is maximum (about 3% compared to prior) near the *CDS* and *OVS* towers. In 2019, a significant reduction in the error was seen in the south of the Paris region, where no towers are located. However, this needs to be investigated further for a definite conclusion. This decrease is co-located with sources from the *others* sector, possibly due to a compensating effect across sectors.

Figure 10 shows the flux maps for the *others* sector. Similar to the *traffic* sector, posterior emissions have increased after inversion more significantly in 2019 (about 38%) compared to 2020 (about 24%), primarily in the central Paris region. A large magnitude of about 150 g CO₂ m⁻² day⁻¹ increase in the emission is seen near the central Paris region, while no change is observed near the north-east and south-west part of the domain where other towers are located. Comparison of 2019 and 2020 posterior emissions shows a decrease of only 21% in the emissions, which is much lower than the traffic emissions discussed above. The most pronounced decline in the *traffic* sector could be a result of the mobility restrictions during the lockdown period. The initial assessment given by AirParif local air quality agency indicates a similar reduction in the *traffic* and *nontraffic* sectors (Lian et al., 2022). Unlike the previous cases, the error reduction is more confined to the center of the Paris metropolitan area (about 10%).

3.2.2. Flux Time Series

Figure 11 shows the 5-day emissions time-series for *traffic* and *others* sectors for 2019 and 2020. The corresponding shaded areas represent their respective uncertainties. In 2019, prior and posterior *traffic* emissions show a nearly constant pattern, whereas *others* emissions show large fluctuations where prior emissions vary between 0.2 and 0.4 MtCO₂ and posterior emissions between 0.3 and 0.7 MtCO₂. Positive readjustment holds valid here only for the *others* emissions. In 2020, the *traffic* emissions were the same as 2019 (2 MtCO₂) at the start of March until decreasing to 0.05 MtCO₂ during the confinement period. This again reaches the previous year's values by the second week of May. Whereas *others* posterior emissions were having a larger magnitude at the beginning of the period, which rapidly reduced during the confinement period. However, the prior emissions show a gradual decrease.

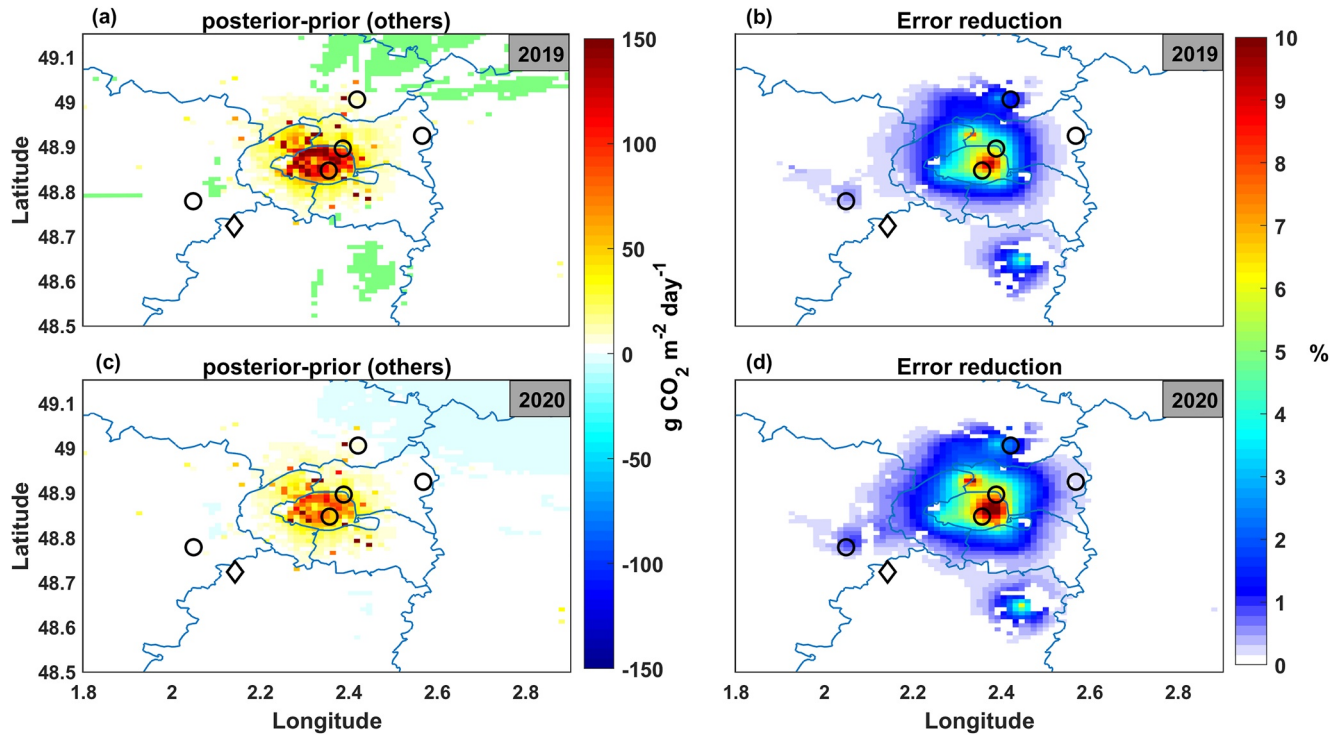


Figure 10. Flux maps of change in emission (day + nighttime) from prior after inversion for the *others* emission sector for (a) 2019 and (c) 2020 and their corresponding error reductions (c and d). Towers used for the inversion are marked as circles and diamond shapes.

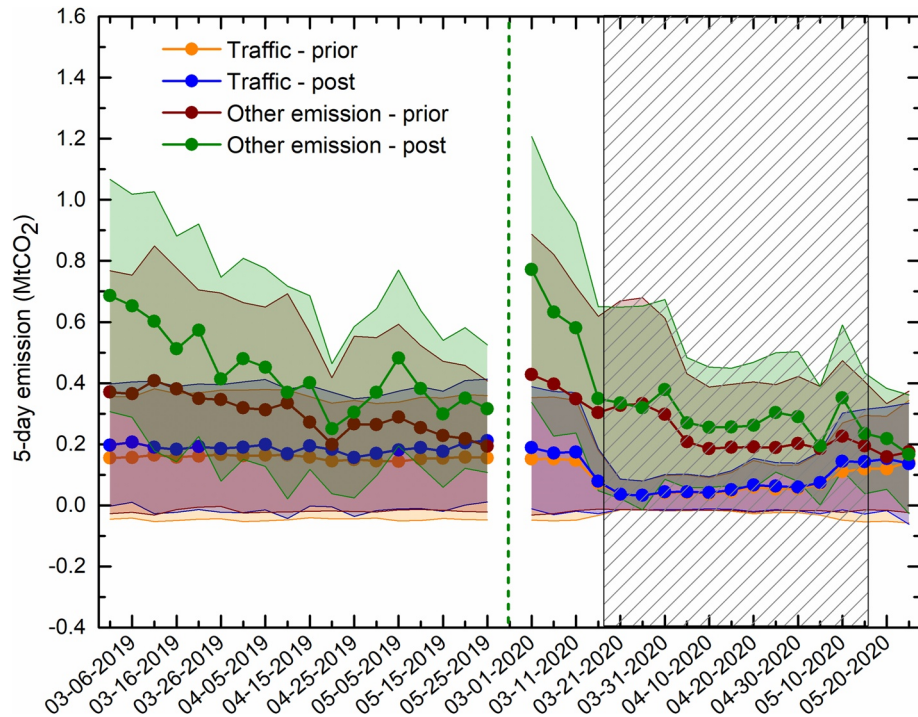


Figure 11. Five-day time series of sectoral (*traffic* and *others*) prior and posterior fossil fuel emissions (day + nighttime) and their respective uncertainties for 2019 and 2020 (colored shaded area). The COVID 19 confinement period is shown as shaded gray zones.

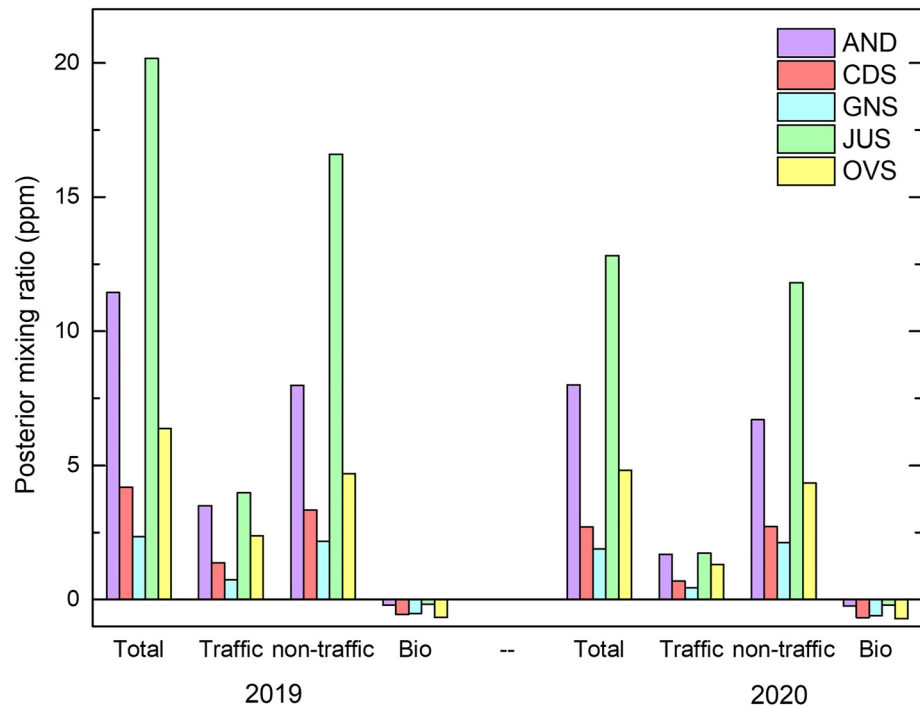


Figure 12. Contribution of different emission sectors and biogenic fluxes to the posterior mixing ratios at the observation towers. The values are mean over the inversion period (March–May).

3.2.3. Sectoral Contributions From Origins.Earth Inventory

This part quantifies the contribution of each sector to the mixing ratio variability over the observation towers. Figure 12 shows the CO_2 mixing ratio contributions from different fossil fuel emission sectors and biogenic fluxes at each tower location based on the posterior emissions and biogenic fluxes combined with the LPDM footprints for 2019 and 2020. The simulated CO_2 mixing ratios correspond to the 1 km surface footprints combined with the 5-day mean posterior emissions, averaged over 3 months for 7–17 UTC. Biogenic fluxes contribute to only a small fraction of the mixing ratio with negative values. For other emission sectors and total contribution, maximum enhancement is seen over *JUS*, a site in the central Paris region, followed by *AND*, *OVS* and *CDS*.

The large enhancement over *AND* despite its 60 m height could be because of emissions in almost every single urban pixel near the site. The *nontraffic* sector is the most significant contributor to the atmospheric enhancements (40% for 2019% and 70% for 2020 of the total enhancements) at all the tower locations, similar to the emission ratios for the same sector (38%). In 2020, there is a reduction in the contribution from *traffic* and *nontraffic* emissions, confirming the overall emission reduction in Paris during the confinement period.

4. Discussion

4.1. Experimental Design for Sensitivity Tests

Several assumptions have been applied to our inversion configuration to evaluate their impacts on the inversion results. We focused on the CO_2 -only inversion configuration, but we expect similar results in the CO-CO_2 inversion results. We evaluated the impact of background, prior errors and correlation length on the inversion, the important components that are expected to influence the inversion system. The consolidated results are shown in Table 2. The reference setup for CO_2 -only and CO-CO_2 inversions presented in shaded rows are defined as (a) the observations from the *SAC* tower are used for the background and (b) the prior error correlation length is defined as 4 km, and (c) the relative prior error variance at the pixel level is set as 100% of the emissions. CO_2 -only inversion is tested for a correlation length of 20 km with the same prior error variance and wind-dependent background mixing ratios. Another test is carried out where prior error variance is set as 60% of the emissions at the pixel level. To test the performance of our inversion system, two tests are carried out where prior emissions of 2019

Table 2
Comparison of Inversion Results for Different Configurations

Inversion		Prior emission (MtCO ₂)	Prior RMSE (MtCO ₂)	Posterior emission (MtCO ₂)	Posterior RMSE (MtCO ₂)	Prior to post change (%)	Reduction ratio (%)		
							prior	post	
Sac background L=4 km, prior error = 100%	2019	4.92	2.37	6.41	2.33	30.56	-37.58	-43.12	
	2020	3.07	1.87	3.65	1.83	18.96			
Sac background L=4 km, prior error = 60%	2019	4.92	1.83	5.75	1.82	17.02	-37.58	-41.39	
	2020	3.07	1.45	3.37	1.43	9.87			
Sac background L=20 km, prior error = 100%	2019	4.92	2.37	8.41	2.11	71.08	-37.58	-46.01	
	2020	3.07	1.87	4.54	1.65	47.96			
wind background L=4 km, prior error = 100%	2019	4.92	2.37	6.61	2.32	34.52	-37.58	-39.99	
	2020	3.07	1.87	3.97	1.83	29.32			
wind background L=20 km, prior error = 100%	2019	4.92	2.37	9.21	2.10	87.42	-37.58	-41.28	
	2020	3.07	1.87	5.41	1.65	76.30			
Sac background L=4 km (prior=2019)	2019	4.91	2.37	6.41	2.33	30.56	0	-11.34	
	2020	4.91	2.37	5.69	2.31	15.75			
Sac background L=4 km (prior=2019, prior error=200%)	2019	4.91	3.35	7.36	3.24	49.77	0	-18.70	
	2020	4.91	3.35	5.98	3.2	21.76			
CO:CO ₂ inversion	traffic	2019	1.68	1.48	1.97	1.47	16.84	-68.27	-70.19
		2020	0.53	0.88	0.59	0.87	9.78		
	others	2019	3.23	1.85	4.48	1.82	38.52	-29.77	-21.59
		2020	2.53	1.65	3.14	1.60	24.07		
CO:CO ₂ inversion (prior=2019)	traffic	2019	1.68	1.48	1.97	1.47	16.84	0	-4.03
		2020	1.68	1.48	1.89	1.47	12.13		
	others	2019	3.23	1.85	4.48	1.82	38.52	0	-14.91
		2020	3.23	1.85	3.81	1.80	17.86		

Note. The reference setup for both the inversions are presented in shaded rows. The ability of our inversion system to capture confinement emission reductions is presented for 2020 using prior emissions of 2019 (rows 6, 7 and 9).

were used for 2020 and prior errors are set to 200% to make the inversion only dependent on observations. In CO-CO₂ inversion, a test is carried out where 2019 prior emissions are used for 2020.

4.1.1. Impact of Prior Errors and Correlation Length on Inverse Emissions

Prior emission errors in high-resolution inversion studies most often lack rigorous and objective quantification. We used two different prior error variances in this study to see their impact on the inversion estimates. Our first variance estimate was equivalent to 40% of the net emissions aggregated over the domain, that is, it was about 100% at the pixel level. Our second experiment uses error variances reduced to 60% of the emissions at the pixel level (~25% over the domain) with a correlation length of 4 km. Despite an increase in the emissions after inversion, the correction after inversion has been reduced by about half compared to the reference inversion for 2019 and 2020. However, the reduction in the posterior emissions from 2019 to 2020 remains almost uniform (-41% instead of -43%). We conclude that the 3-month inverse emissions are highly sensitive to the choice of prior error variances, while the relative decrease in emissions from 2019 to 2020 due to the restrictions (confinement) is nearly insensitive.

Figure 13 shows the difference between the posterior and prior emissions and the error reduction for a large correlation length of 20 km (while keeping the other parameters identical to our reference inversion configuration). Here the spatial extent of the emissions corrections increased dramatically compared to the reference inversion in Figure 4. It is evident that the prior emission error structures play a major role in the spatial distribution of

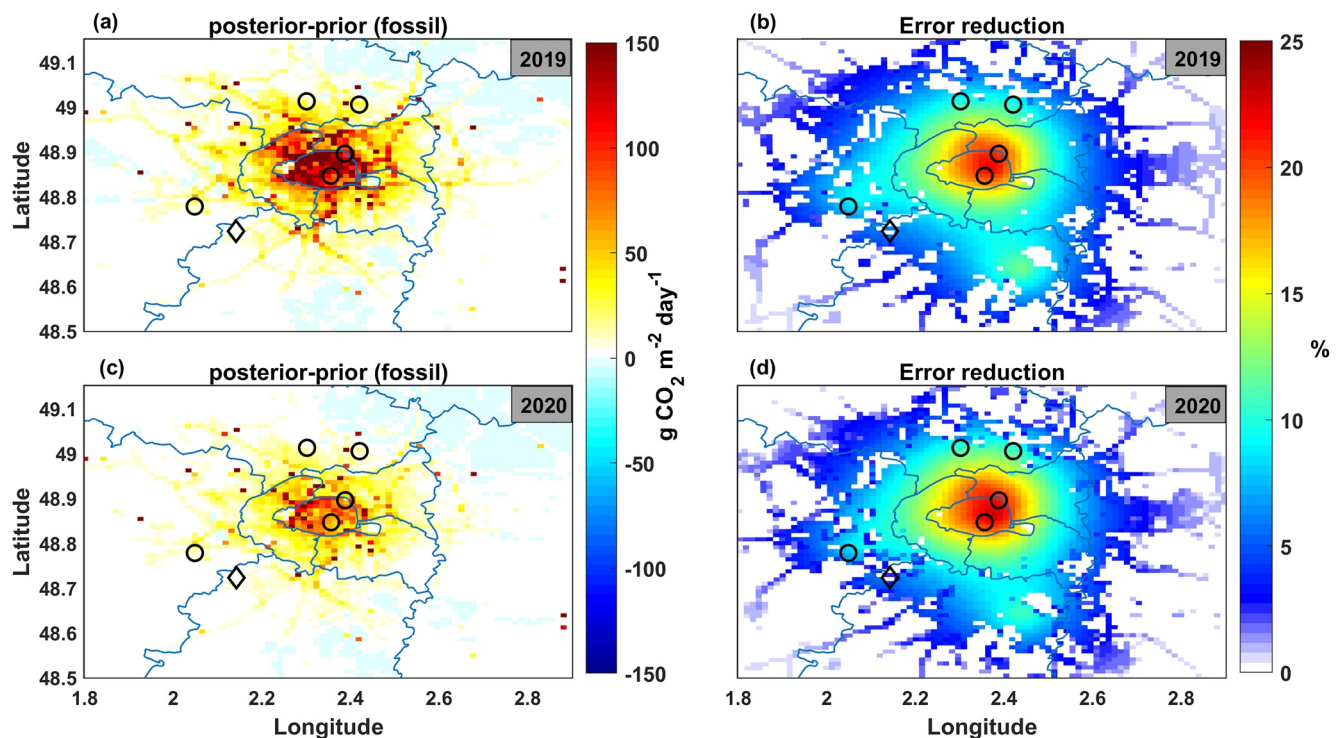


Figure 13. Day-time total fossil fuel emission change for (a) 2019 and (c) 2020, and their corresponding error reductions (b and d) using 20 km correlation length.

the flux corrections. Similarly, the posterior emissions increased by about 71% for 2019% and 47% for 2020. However, the emission reduction ratio from 2019 to 2020 remains identical to our reference inversion (only a 3% change). It implies that the relative decrease in posterior emissions between 2019 and 2020 is fairly robust, irrespective of our input parameters (i.e., both error correlation and variances).

The error reduction follows a similar pattern covering a larger area with values reaching up to 25%. The spatial pattern is more circular, a direct consequence of the exponentially-decaying error correlation, with the largest values in the center of the inversion domain. The error reduction shows similar pattern in 2019 and 2020. We conclude here that mapping the spatial distribution of the emissions will require additional information related to the spatial correlations of the inventory uncertainties or additional measurement locations to constrain the full extent of the metropolitan area. However, the relative impact of the confinement on fossil fuel emissions remains robust to our inversion configuration assumptions.

4.1.2. Impact of Background on Inversion

The methodology used to compute hourly background values by assimilating local enhancements relative to a specified background is one of the major assumptions made in our inversion system. Biases associated with the selection of background mixing ratios will be propagated to the posterior flux estimation. Selecting background mixing ratios from the upwind tower network is potentially less representative than using spatially resolved modeled values. However, Bréon et al. (2015) pointed out that for the city-scale inversion, current regional models would fail to provide sufficient accuracy while using spatially resolved modeled values. Several other studies have discussed the impact of background mixing ratios on inversion (e.g., Lauvaux et al., 2016; Miles et al., 2021; Mueller et al., 2018; Pisso et al., 2019; Turnbull et al., 2015). Here, we present the results from different strategies used to define the background values.

In the first method, hourly mixing ratios from *SAC* at the exact time of the observations is used as the background mixing ratios for inversion and presented as the reference case. For about 60% of the time, *SAC* acts as an upwind site. In the second method, the optimal site location is identified based on the domain-averaged wind direction. *SAC* and *AND* are the two most viable options (no large nearby sources) but can be influenced by the local vegetation. We note here that if the observations from one site are unavailable, observations from the other are used

even if the wind direction is not optimal. The inversion results are consolidated in Table 2 for two different correlation lengths (4 and 20 km). In the reference set up, using *SAC* and *AND* as background stations, the posterior emissions show an increase of about 35% and 30% in 2019 and 2020, respectively. By comparison, when using *SAC* alone to define the background, the increase was about 30% and 19%, respectively. This correction increases further to about 50% for 20 km correlation length, as seen in our reference inversion test case. However, the emission reduction during confinement is almost the same for both the cases and to the reference case discussed above. We conclude here that the choice of the background station has a noticeable impact on the 3-month emissions estimates. However, this impact remains lower than the impact of the prior error correlation length.

4.1.3. Sensitivity of the Prior Inventory

To test whether the existing observations are sufficient to capture the emission reduction per sector during the lockdown period, Two tests are performed for CO₂-only inversion and one test for CO-CO₂ inversion during March-May 2020 but using the 2019 prior emissions. The results are shown in the sixth, seventh, and last rows of Table 2. Compared with the reference CO₂-only inversion, a 10% increase in the emissions was seen after inversion (row representing 2020). On the other hand, emission reduction from 2019 to 2020 associated with the COVID 19 lockdown shows only a 11% difference, much lower than the original reduction (−43%) in the reference inversion. The remaining 30% reduction would be the reduction represented in the Origins.Earth inventory itself. One of the reasons for the poor sensitivity of our inversion system could be because the towers in the city center (*CDS*) are not capturing the emissions from the city. However, we need to analyze this further to derive conclusions.

To test the sensitivity of observations alone to the inversion, an additional sensitivity test has been done where prior errors are set to 200% of emissions. Emissions have increased after inversion by 50% and 21% for 2019 and 2020 respectively compared to the prior emissions. With the same prior emissions (of 2019) in 2020, an emission reduction of 18.7% has resulted. Though it is still a small contribution compared to the impact of priors, the observations are indeed adding a significant contribution to the results. Compared with the reference CO-CO₂ inversion (row 8), the prior-to-posterior emission change increased from 14% to 20% for *traffic* emissions, whereas it decreased by about 15% for the *others* sector. On the other hand, the emission reduction from 2019 to 2020 for the *traffic* sector shows a reduction of only 4%, much lower than the original reduction (−70%) in the reference inversion. Compared with the reference CO₂-only inversion, the *traffic* emissions decreased by about 68%, whereas the *others* sector showed a reduction of only 30%. We conclude that the 2019 to 2020 emission reduction is only partially captured by the atmospheric observations alone (−14% instead of −44%). At the sectoral level, the decrease in *traffic* emissions (in the reference inversion) is almost entirely driven by the assumed decrease in the 2020 prior emissions, while the *others* sector decreases by only 14% (compared to 21% in the reference inversion). The *others* sector represents a larger fraction of the city emissions, hence has been assigned larger uncertainties. This implies that the actual sectoral reductions due to the confinement are not well-constrained by the CO observations. However, our results are consistent with previous studies (Nathan et al., 2018). We conclude here that additional tracers for both sectors are needed to separate sectoral emissions over the city of Paris (e.g., NO_x).

5. Conclusions

Our study presents fossil fuel emissions estimates from a high-resolution Bayesian inversion system at 1 km resolution over the Paris metropolitan area. The inversion is carried out during the spring season (March-May) of 2019 and 2020 using a priori emissions from the Origins.Earth inventory and biogenic fluxes from the VPRM model. Biogenic fluxes remained nearly constant and small during the March-May period, possibly due to our tower gradient approach, which excludes most non-local sources and sinks, or due to the low fluxes from VPRM (hence low prior errors compared to the fossil fuel contribution). However, a significant increase (about 150 g CO₂ m^{−2} day^{−1}) in the fossil fuel emissions was resulted in the central Paris region across all our inversion experiments. Prior emission errors were reduced by up to 15% after inversion in the center of Paris. Flux time series shows a noticeable enhancement in the posterior emissions with large 5-day variations. Across multiple sensitivity experiments, we quantified the relative impact of the first confinement period due to the COVID 19 pandemic on the fossil fuel CO₂ emissions over Paris. The estimated impact of COVID 19 confinement on the emissions was about −37% to −46% (reduction) depending on the configuration of the inversion system. However, 3-month

emissions estimates varied significantly depending on the inversion configuration, starting with the uncertainties in the emissions inventory (prior error variances and correlations).

The large reduction after the initial weeks of March in 2020 coincides with the COVID 19 lockdown restrictions, which considerably reduced most of the fuel-based activities across the Paris region. We combined CO and CO₂ mole fractions to quantify the fossil fuel CO₂ emissions from *traffic* (on-road and off-road) and *nontraffic (others)* sectors separately. The inversion shows an increase in the *traffic* emissions from the high-resolution inventory by about 17% over the Paris metropolitan area in 2019 and by about 10% in 2020. Emissions from the *other* sectors also increased significantly in 2019 (about 38%) and 2020 (about 24%), primarily within downtown Paris. The overall results for the emission over the lockdown period show limited sensitivity to our inversion setup but significant to the prior fluxes. The configuration tends to increase the fossil fuel CO₂ emission with respect to the prior emissions for 2019 and 2020, which gives us the impression that the prior emissions were underestimated. However, the joint assimilation of CO with CO₂ mixing ratios was of limited use to separate the two sectors. We also identified that the lack of information relative to inventory uncertainties remains a major limitation in quantifying the aggregated 3-month emissions for both years. While the relative 2019 to 2020 reduction (caused primarily by lockdown restrictions) is robust to prior errors, we found large differences in our inverse emissions due to prior error correlation structures and due to prior error variances. We also identified background mixing ratios as the second most critical assumption. Therefore, precise mapping of fossil fuel emissions at the urban scale will require additional information to quantify both the high-resolution inventory errors and their spatial structures. However, through the inversion we found the impact of lockdown restrictions on CO₂ fossil fuel emissions to an additional reduction of -12% ($\pm 4\%$) over the Paris metropolitan area, compared to the reduction estimated by the prior inventory.

Data Availability Statement

The observation data from the six towers of the French monitoring network for greenhouse gases were used to perform the inversion study. The filtered data used in the model simulations are available to the readers as the netcdf files in the repository <https://zenodo.org/account/settings/github/repository/nalkrishna/Inversionoutputs#> (<https://doi.org/10.5281/zenodo.6804555>). Hourly observation fields used in the model-data comparison and inversion for 2019–2020 are available as text files in the repository <https://zenodo.org/account/settings/github/repository/nalkrishna/GHG-data#> (<https://doi.org/10.5281/zenodo/6806644>). All the data from the Ile de France network will be released to the public after different levels of quality checks through AERIS data centre, which could be accessed via [aeris – Data and Services for the Atmosphere \(aeris-data.fr\)](https://aeris-data.fr). CO₂ and CO emissions are taken from the inventories TNO ([Emissions | TNO](https://www.tno.nl/en/our-work/energy-emissions)) and Origins.Earth ([Origins.earth: system for monitoring CO2 emissions and access to climate finance](https://www.origins-earth.com/)). Data analysis is done with Matlab version 2019 (MATLAB and Statistics Toolbox Release, 2019; [MATLAB Login | MATLAB & Simulink \(mathworks.com\)](https://www.mathworks.com/))).

Acknowledgments

K. Nalini, P. Ciais, C. Abdallah, and T. Lauvaux were supported by the French program Make Our Planet Great Again (project CIUDAD, CNRS). We acknowledge the French monitoring network for greenhouse gases (SNO-IFA) coordinated by LSCE-OVSQ (M. Ramonet and O. Laurent) for providing the data for the study. K. Nalini performed the inversions using the inversion system developed by T. Lauvaux. J. Lian performed the WRF-Chem model outputs for the LPDM simulations and inversion; C. Abdallah provided the LPDM trajectory outputs; H. Utard developed and prepared the Origins.Earth emission product. P. Ciais provided comments and discussed the results of the study.

References

- Ahmadov, R., Gerbig, C., Kretschmer, R., Koerner, S., Neining, B., Dolman, A. J., & Sarrat, C. (2007). Mesoscale covariance of transport and CO₂ fluxes: Evidence from observations and simulations using the WRF-VPRM coupled atmosphere-biosphere model. *Journal of Geophysical Research*, *112*(D22), D22107. <https://doi.org/10.1029/2007jd008552>
- Ahmadov, R., Gerbig, C., Kretschmer, R., Körner, S., Rödenbeck, C., Bousquet, P., & Ramonet, M. (2009). Comparing high resolution WRF-VPRM simulations and two global CO₂ transport models with coastal tower measurements of CO₂. *Biogeosciences*, *6*(5), 807–817. <https://doi.org/10.5194/bg-6-807-2009>
- Airparif (2013). Bilan des Émissions de Polluants Atmosphériques et de Gaz à Effet de Serre en Île-de-France pour l'Année 2010 et Historique 2000/05: Méthodologie et résultats. Retrieved from http://www.airparif.asso.fr/_pdf/publications/%20Emissions_2010_CG75.pdf May 2014.
- Ammoura, L., Xueref-Remy, I., Gros, V., Baudic, A., Bonsang, B., Petit, J. E., et al. (2014). Atmospheric measurements of ratios between CO₂ and co-emitted species from traffic: A tunnel study in the Paris megacity. *Atmospheric Chemistry and Physics*, *14*(23), 12871–12882. <https://doi.org/10.5194/acp-14-12871-2014>
- Ammoura, L., Xueref-Remy, I., Vogel, F., Gros, V., Baudic, A., Bonsang, B., et al. (2016). Exploiting stagnant conditions to derive robust emission ratio estimates for CO₂, CO and volatile organic compounds in Paris. *Atmospheric Chemistry and Physics*, *16*(24), 15653–15664. <https://doi.org/10.5194/acp-16-15653-2016>
- Arioli, M. S., Márcio de Almeida, D. A., Amaral, F. G., & Cybis, H. B. B. (2020). The evolution of city-scale GHG emissions inventory methods: A systematic review. *Environmental Impact Assessment Review*, *80*, 106316. <https://doi.org/10.1016/j.eiar.2019.106316>
- Berrisford, P., Dee, D. P., Fielding, K., Fuentes, M., Kallberg, P., Kobayashi, S., et al. (2009). The ERA-interim archive. *ERA Report Series*, (1), 1–16.
- Bousquet, P., Ciais, P., Peylin, P., Ramonet, M., & Monfray, P. (1999). Inverse modeling of annual atmospheric CO₂ sources and sinks: 1. Method and control inversion. *Journal of Geophysical Research*, *104*(D21), 26161–26178. <https://doi.org/10.1029/1999jd900342>

- Bréon, F. M., Broquet, G., Puygrenier, V., Chevallier, F., Xueref-Remy, I., Ramonet, M., et al. (2015). An attempt at estimating Paris area CO₂ emissions from atmospheric concentration measurements. *Atmospheric Chemistry and Physics*, *15*(4), 1707–1724. <https://doi.org/10.5194/acp-15-1707-2015>
- Brunner, D., Arnold, T., Henne, S., Manning, A., Thompson, R. L., Maione, M., et al. (2017). Comparison of four inverse modelling systems applied to the estimation of HFC-125, HFC-134a, and SF₆ emissions over Europe. *Atmospheric Chemistry and Physics*, *17*(17), 10651–10674. <https://doi.org/10.5194/acp-17-10651-2017>
- Chen, F., & Dudhia, J. (2001). Coupling an advanced land surface–hydrology model with the Penn State–NCAR MM5 Modeling system. Part II: Preliminary model validation. *Monthly Weather Review*, *129*(4), 587–604. [https://doi.org/10.1175/1520-0493\(2001\)129<0587:caalsh>2.0.co;2](https://doi.org/10.1175/1520-0493(2001)129<0587:caalsh>2.0.co;2)
- Ciais, P., Rayner, P., Chevallier, F., Bousquet, P., Logan, M., Peylin, P., et al. (2010). Atmospheric inversions for estimating CO₂ fluxes: Methods and perspectives. In *Greenhouse gas inventories* (pp. 69–92). Springer.
- Colville, R. N., Hutchinson, E. J., Mindell, J. S., & Warren, R. F. (2001). The transport sector as a source of air pollution. *Atmospheric Environment*, *35*(9), 1537–1565. [https://doi.org/10.1016/s1352-2310\(00\)00551-3](https://doi.org/10.1016/s1352-2310(00)00551-3)
- Duncan, B. N., Logan, J. A., Bey, I., Megretskaia, I. A., Yantosca, R. M., Novelli, P. C., et al. (2007). Global budget of CO, 1988–1997: Source estimates and validation with a global model. *Journal of Geophysical Research*, *112*(D22), D22301. <https://doi.org/10.1029/2007jd008459>
- Eggleston, S., Buendia, L., Miwa, K., Ngara, T., & Tanabe, K. (2006). IPCC guidelines for national greenhouse gas inventories.
- Enting, I. G. (2002). *Inverse problems in atmospheric constituent transport*. Cambridge University Press.
- Feng, S., Lauvaux, T., Newman, S., Rao, P., Ahmadov, R., Deng, A., et al. (2016). Los Angeles megacity: A high-resolution land–atmosphere modeling system for urban CO₂ emissions. *Atmospheric Chemistry and Physics*, *16*(14), 9019–9045. <https://doi.org/10.5194/acp-16-9019-2016>
- Geels, C., Andersen, H. V., Ambelas Skjøth, C., Christensen, J. H., Ellermann, T., Løfstrøm, P., et al. (2012). Improved modelling of atmospheric ammonia over Denmark using the coupled modelling system DAMOS. *Biogeosciences*, *9*(7), 2625–2647. <https://doi.org/10.5194/bg-9-2625-2012>
- Gerbig, C., Lin, J. C., Wofsy, S. C., Daube, B. C., Andrews, A. E., Stephens, B. B., et al. (2003). Toward constraining regional-scale fluxes of CO₂ with atmospheric observations over a continent: 2. Analysis of COBRA data using a receptor-oriented framework. *Journal of Geophysical Research*, *108*(D24), 4757. <https://doi.org/10.1029/2003jd003770>
- Goeckede, M., Yadav, V., Michalak, A. M., & Law, B. E. (2010). *Evaluating the role of prior information in atmospheric inverse modeling frameworks through comparison with geostatistical inverse modeling techniques*. AGU Fall Meeting Abstracts, (Vol. 2010, pp. B31F–0367).
- Gourdji, S. M., Karion, A., Lopez-Coto, I., Ghosh, S., Mueller, K. L., Zhou, Y., et al. (2022). A modified Vegetation Photosynthesis and Respiration Model (VPRM) for the eastern USA and Canada, evaluated with comparison to atmospheric observations and other biospheric models. *Journal of Geophysical Research: Biogeosciences*, *127*(1), e2021JG006290. <https://doi.org/10.1029/2021jg006290>
- Griffin, R. J., Chen, J., Carmody, K., Vutukuru, S., & Dabdub, D. (2007). Contribution of gas phase oxidation of volatile organic compounds to atmospheric carbon monoxide levels in two areas of the United States. *Journal of Geophysical Research*, *112*(D10), D10S17. <https://doi.org/10.1029/2006jd007602>
- Guenther, A., Hewitt, C. N., Erickson, D., Fall, R., Geron, C., Graedel, T., et al. (1995). A global model of natural volatile organic compound emissions. *Journal of Geophysical Research*, *100*(D5), 8873–8892. <https://doi.org/10.1029/94jd02950>
- Gurney, K. R., Law, R. M., Denning, A. S., Rayner, P. J., Baker, D., Bousquet, P., et al. (2002). Towards robust regional estimates of CO₂ sources and sinks using atmospheric transport models. *Nature*, *415*(6872), 626–630. <https://doi.org/10.1038/415626a>
- Gurney, K. R., Law, R. M., Denning, A. S., Rayner, P. J., Baker, D., Bousquet, P., et al. (2003). TransCom 3 CO₂ inversion intercomparison: 1. Annual mean control results and sensitivity to transport and prior flux information. *Tellus B: Chemical and Physical Meteorology*, *55*(2), 555–579. <https://doi.org/10.1034/j.1600-0889.2003.00049.x>
- Gurney, K. R., Liang, J., Roest, G., Song, Y., Mueller, K., & Lauvaux, T. (2021). Under-reporting of greenhouse gas emissions in US cities. *Nature Communications*, *12*(1), 1–7. <https://doi.org/10.1038/s41467-020-20871-0>
- Hazan, L., Tarniewicz, J., Ramonet, M., Laurent, O., & Abbaris, A. (2016). Automatic processing of atmospheric CO₂ and CH₄ mole fractions at the ICOS atmosphere thematic centre. *Atmospheric Measurement Techniques*, *9*, 4719–4736. <https://doi.org/10.5194/amt-9-4719-2016>
- Heimann, M., & Kaminski, T. (1999). Inverse modelling approaches to infer surface trace gas fluxes from observed atmospheric mixing ratios. *Developments in Atmospheric Science*, (Vol. 24, pp. 277–295). Elsevier.
- Holloway, T., Levy, H., & Kasibhatla, P. (2000). Global distribution of carbon monoxide. *Journal of Geophysical Research*, *105*(D10), 12123–12147. <https://doi.org/10.1029/1999jd901173>
- Hsu, A., Höhne, N., Kuramochi, T., Roelfsema, M., Weinfurter, A., Xie, Y., et al. (2019). A research roadmap for quantifying non-state and subnational climate mitigation action. *Nature Climate Change*, *9*(1), 11–17. <https://doi.org/10.1038/s41558-018-0338-z>
- Hu, L., Montzka, S. A., Miller, B. R., Andrews, A. E., Miller, J. B., Lehman, S. J., et al. (2016). Continued emissions of carbon tetrachloride from the United States nearly two decades after its phaseout for dispersive uses. *Proceedings of the National Academy of Sciences*, *113*(11), 2880–2885. <https://doi.org/10.1073/pnas.1522284113>
- Hutyra, L. R., Duren, R., Gurney, K. R., Grimm, N., Kort, E. A., Larson, E., & Shrestha, G. (2014). Urbanization and the carbon cycle: Current capabilities and research outlook from the natural sciences perspective. *Earth's Future*, *2*(10), 473–495. <https://doi.org/10.1002/2014ef000255>
- IPCC. (2006). *IPCC guidelines for national greenhouse gas inventories, prepared by the national greenhouse gas inventories programme*. IGES.
- Janjić, Z. I. (1990). The step-mountain coordinate: Physical package. *Monthly Weather Review*, *118*(7), 1429–1443. [https://doi.org/10.1175/1520-0493\(1990\)118<1429:tscmpp>2.0.co;2](https://doi.org/10.1175/1520-0493(1990)118<1429:tscmpp>2.0.co;2)
- Janjić, Z. I. (1994). The step-mountain eta coordinate model: Further developments of the convection, viscous sublayer, and turbulence closure schemes. *Monthly Weather Review*, *122*(5), 927–945. [https://doi.org/10.1175/1520-0493\(1994\)122<0927:tscmcm>2.0.co;2](https://doi.org/10.1175/1520-0493(1994)122<0927:tscmcm>2.0.co;2)
- Janjić, Z. I. (1996). *The Mellor-Yamada level 2.5 turbulence closure scheme in the NCEP Eta Model* (pp. 4–14). World Meteorological Organization-Publications-WMO TD.
- Jung, M., Henkel, K., Herold, M., & Churkina, G. (2006). Exploiting synergies of global land cover products for carbon cycle modeling. *Remote Sensing of Environment*, *101*(4), 534–553. <https://doi.org/10.1016/j.rse.2006.01.020>
- Kaminski, T., Heimann, M., & Giering, R. (1999). A coarse grid three-dimensional global inverse model of the atmospheric transport: 1. Adjoint model and Jacobian matrix. *Journal of Geophysical Research*, *104*(D15), 18535–18553. <https://doi.org/10.1029/1999jd900147>
- Kaminski, T., Rayner, P. J., Heimann, M., & Enting, I. G. (2001). On aggregation errors in atmospheric transport inversions. *Journal of Geophysical Research*, *106*(D5), 4703–4715. <https://doi.org/10.1029/2000jd900581>
- Karion, A., Sweeney, C., Kort, E. A., Shepson, P. B., Brewer, A., Cambaliza, M., et al. (2015). Aircraft-based estimate of total methane emissions from the Barnett Shale region. *Environmental Science & Technology*, *49*(13), 8124–8131. <https://doi.org/10.1021/acs.est.5b00217>
- Kort, E. A., Angevine, W. M., Duren, R., & Miller, C. E. (2013). Surface observations for monitoring urban fossil fuel CO₂ emissions: Minimum site location requirements for the Los Angeles megacity. *Journal of Geophysical Research: Atmospheres*, *118*(3), 1577–1584. <https://doi.org/10.1002/jgrd.50135>

- Laurent, O., Philippon, C., Yver Kwok, C., Rivier, L., & Ramonet, M. (2019). How to deal with water vapor for Greenhouse gas dry mole fraction measurement with cavity enhanced spectrometer. In *Other greenhouse gases and related measurement techniques (GGMT-2019), jeju island, South Korea, 2–5 September 2019* GAW report 25. 20th WMO/IAEA Meeting on Carbon Dioxide.
- Lauvaux, T., Gurney, K. R., Miles, N. L., Davis, K. J., Richardson, S. J., Deng, A., et al. (2020). Policy-relevant assessment of urban CO₂ emissions. *Environmental Science & Technology*, *54*(16), 10237–10245. <https://doi.org/10.1021/acs.est.0c00343>
- Lauvaux, T., Miles, N. L., Deng, A., Richardson, S. J., Cambaliza, M. O., Davis, K. J., et al. (2016). High-resolution atmospheric inversion of urban CO₂ emissions during the dormant season of the Indianapolis Flux Experiment (INFLUX). *Journal of Geophysical Research: Atmospheres*, *121*(10), 5213–5236. <https://doi.org/10.1002/2015jd024473>
- Lauvaux, T., Schuh, A. E., Uliasz, M., Richardson, S., Miles, N., Andrews, A. E., et al. (2012). Constraining the CO₂ budget of the corn belt: Exploring uncertainties from the assumptions in a mesoscale inverse system. *Atmospheric Chemistry and Physics*, *12*(1), 337–354. <https://doi.org/10.5194/acp-12-337-2012>
- Lauvaux, T., Uliasz, M., Sarraz, C., Chevallier, F., Bousquet, P., Lac, C., et al. (2008). Mesoscale inversion: First results from the CERES campaign with synthetic data. *Atmospheric Chemistry and Physics*, *8*(13), 3459–3471. <https://doi.org/10.5194/acp-8-3459-2008>
- Law, R. M., Chen, Y. H., Gurney, K. R., & 3 Modellers, T. (2003). TransCom 3 CO₂ inversion intercomparison: 2. Sensitivity of annual mean results to data choices. *Tellus B: Chemical and Physical Meteorology*, *55*(2), 580–595. <https://doi.org/10.1034/j.1600-0889.2003.00053.x>
- Levin, I., & Karstens, U. T. E. (2007). Inferring high-resolution fossil fuel CO₂ records at continental sites from combined ¹⁴C and CO observations. *Tellus B: Chemical and Physical Meteorology*, *59*(2), 245–250. <https://doi.org/10.3402/tellusb.v59i2.16985>
- Levin, I., Kromer, B., Schmidt, M., & Sartorius, H. (2003). A novel approach for independent budgeting of fossil fuel CO₂ over Europe by ¹⁴C observations. *Geophysical Research Letters*, *30*(23), 2194. <https://doi.org/10.1029/2003gl018477>
- Lian, J., Bréon, F. M., Broquet, G., Lauvaux, T., Zheng, B., Ramonet, M., et al. (2021). Sensitivity to the sources of uncertainties in the modeling of atmospheric CO₂ concentration within and in the vicinity of Paris. *Atmospheric Chemistry and Physics*, *21*(13), 10707–10726. <https://doi.org/10.5194/acp-21-10707-2021>
- Lian, J., Bréon, F. M., Broquet, G., Zaccheo, T. S., Dobler, J., Ramonet, M., et al. (2019). Analysis of temporal and spatial variability of atmospheric CO₂ concentration within Paris from the GreenLITE™ laser imaging experiment. *Atmospheric Chemistry and Physics*, *19*(22), 13809–13825. <https://doi.org/10.5194/acp-19-13809-2019>
- Lian, J., Lauvaux, T., Utard, H., Broquet, G., Broquet, G., Bréon, F. M., et al. (2022). Assessing the effectiveness of an urban CO₂ monitoring network through the COVID-19 lockdown natural experiment. *Environmental Science & Technology*, *56*(4), 2153–2162. <https://doi.org/10.1021/acs.est.1c04973>
- Lian, J., Wu, L., Bréon, F. M., Broquet, G., Vautard, R., Zaccheo, T. S., et al. (2018). Evaluation of the WRF-UCM mesoscale model and ECMWF global operational forecasts over the Paris region in the prospect of tracer atmospheric transport modeling. *Elementa: Science of the Anthropocene*, *6*. <https://doi.org/10.1525/elementa.319>
- Lin, J. C., Gerbig, C., Wofsy, S. C., Andrews, A. E., Daube, B. C., Davis, K. J., et al. (2003). A near-field tool for simulating the upstream influence of atmospheric observations: The Stochastic Time-Inverted Lopez Lagrangian Transport (STILT) model. *Journal of Geophysical Research*, *108*(D16), ACH2-1–ACH2-17. <https://doi.org/10.1029/2002jd003161>
- Lopez, M., Schmidt, M., Delmotte, M., Colomb, A., Gros, V., Janssen, C., et al. (2013). CO, NO_x and ¹³C as tracers for fossil fuel CO₂: Results from a pilot study in Paris during winter 2010. *Atmospheric Chemistry and Physics*, *13*(15), 7343–7358. <https://doi.org/10.5194/acp-13-7343-2013>
- Lopez-Coto, I., Ren, X., Salmon, O. E., Karion, A., Shepson, P. B., Dickerson, R. R., et al. (2020). Wintertime CO₂, CH₄, and CO emissions estimation for the Washington, DC–Baltimore metropolitan area using an inverse modeling technique. *Environmental Science & Technology*, *54*(5), 2606–2614. <https://doi.org/10.1021/acs.est.9b06619>
- Mahadevan, P., Wofsy, S. C., Matross, D. M., Xiao, X., Dunn, A. L., Lin, J. C., et al. (2008). A satellite-based biosphere parameterization for net ecosystem CO₂ exchange: Vegetation Photosynthesis and Respiration Model (VPRM). *Global Biogeochemical Cycles*, *22*(2). <https://doi.org/10.1029/2006gb002735>
- Maiss, M., & Brenninkmeijer, C. A. (1998). Atmospheric SF₆: Trends, sources, and prospects. *Environmental Science & Technology*, *32*(20), 3077–3086. <https://doi.org/10.1021/es9802807>
- Manning, A. J., Ryall, D. B., Derwent, R. G., Simmonds, P. G., & O'Doherty, S. (2003). Estimating European emissions of ozone-depleting and greenhouse gases using observations and a modeling back-attribution technique. *Journal of Geophysical Research*, *108*(D14), 4405. <https://doi.org/10.1029/2002jd002312>
- Martilli, A., Clappier, A., & Rotach, M. W. (2002). An urban surface exchange parameterisation for mesoscale models. *Boundary-Layer Meteorology*, *104*(2), 261–304. <https://doi.org/10.1023/a:1016099921195>
- MATLAB & Statistics Toolbox Release. (2019). The MathWorks, Inc.
- McKain, K., Wofsy, S. C., Nehrkorn, T., Eluszkiewicz, J., Ehleringer, J. R., & Stephens, B. B. (2012). Assessment of ground-based atmospheric observations for verification of greenhouse gas emissions from an urban region. *Proceedings of the National Academy of Sciences*, *109*(22), 8423–8428. <https://doi.org/10.1073/pnas.1116645109>
- Meijer, H. A. J., Smid, H. M., Perez, E., & Keizer, M. G. (1996). Isotopic characterisation of anthropogenic CO₂ emissions using isotopic and radiocarbon analysis. *Physics and Chemistry of the Earth*, *21*(5–6), 483–487. [https://doi.org/10.1016/s0079-1946\(97\)81146-9](https://doi.org/10.1016/s0079-1946(97)81146-9)
- Miles, N. L., Davis, K. J., Richardson, S. J., Lauvaux, T., Martins, D. K., Deng, A. J., et al. (2021). The influence of near-field fluxes on seasonal carbon dioxide enhancements: Results from the Indianapolis flux experiment (INFLUX). *Carbon Balance and Management*, *16*(1), 1–15. <https://doi.org/10.1186/s13021-020-00166-z>
- Miller, J. B., Lehman, S. J., Montzka, S. A., Sweeney, C., Miller, B. R., Karion, A., et al. (2012). Linking emissions of fossil fuel CO₂ and other anthropogenic trace gases using atmospheric ¹⁴C. *Journal of Geophysical Research*, *117*(D8), D08302. <https://doi.org/10.1029/2011jd017048>
- Miller, J. B., Lehman, S. J., Verhulst, K. R., Miller, C. E., Duren, R. M., Yadav, V., et al. (2020). Large and seasonally varying biospheric CO₂ fluxes in the Los Angeles megacity revealed by atmospheric radiocarbon. *Proceedings of the National Academy of Sciences*, *117*(43), 26681–26687. <https://doi.org/10.1073/pnas.2005253117>
- Mueller, J. T., McConnell, K., Burrow, P. B., Pofahl, K., Merdjanoff, A. A., & Farrell, J. (2021). Impacts of the COVID-19 pandemic on rural America. *Proceedings of the National Academy of Sciences*, *118*(1). <https://doi.org/10.1073/pnas.2019378118>
- Mueller, K., Yadav, V., Lopez-Coto, I., Karion, A., Gourdji, S., Martin, C., & Whetstone, J. (2018). Siting background towers to characterize incoming air for urban greenhouse gas estimation: A case study in the Washington, DC/Baltimore area. *Journal of Geophysical Research: Atmospheres*, *123*(5), 2910–2926. <https://doi.org/10.1002/2017jd027364>
- Nathan, B. J., Lauvaux, T., Turnbull, J. C., Richardson, S. J., Miles, N. L., & Gurney, K. R. (2018). Source sector attribution of CO₂ emissions using an urban CO/CO₂ Bayesian inversion system. *Journal of Geophysical Research: Atmospheres*, *123*(23), 13–611. <https://doi.org/10.1029/2018jd029231>

- Newman, S., Xu, X., Gurney, K. R., Hsu, Y. K., Li, K. F., Jiang, X., et al. (2016). Toward consistency between trends in bottom-up CO₂ emissions and top-down atmospheric measurements in the Los Angeles megacity. *Atmospheric Chemistry and Physics*, *16*(6), 3843–3863. <https://doi.org/10.5194/acp-16-3843-2016>
- Nickless, A., Rayner, P. J., Engelbrecht, F., Brunke, E. G., Erni, B., & Scholes, R. J. (2018). Estimates of CO₂ fluxes over the city of Cape town, South Africa, through Bayesian inverse modelling. *Atmospheric Chemistry and Physics*, *18*(7), 4765–4801. <https://doi.org/10.5194/acp-18-4765-2018>
- Oda, T., Lauvaux, T., Lu, D., Rao, P., Miles, N. L., Richardson, S. J., & Gurney, K. R. (2017). On the impact of granularity of space-based urban CO₂ emissions in urban atmospheric inversions: A case study for Indianapolis. *Elementa: Science of the Anthropocene*, *5*. <https://doi.org/10.1525/elementa.146>
- Oda, T., Maksyutov, S., & Andres, R. J. (2018). The open-source data inventory for anthropogenic CO₂, version 2016 (ODIAC2016): A global monthly fossil fuel CO₂ gridded emissions data product for tracer transport simulations and surface flux inversions. *Earth System Science Data*, *10*(1), 87–107. <https://doi.org/10.5194/essd-10-87-2018>
- Oney, B., Gruber, N., Henne, S., Leuenberger, M., & Brunner, D. (2017). A CO₂-based method to determine the regional biospheric signal in atmospheric CO₂. *Tellus B: Chemical and Physical Meteorology*, *69*(1), 1353388. <https://doi.org/10.1080/16000889.2017.1353388>
- Pachauri, R. K., Allen, M. R., Barros, V. R., Broome, J., Cramer, W., Christ, R., et al. (2014). *Climate change 2014: Synthesis report. Contribution of working groups I, II and III to the fifth assessment report of the intergovernmental panel on climate change* (p. 151). Ipcc.
- Pal, S., Xueref-Remy, I., Ammoura, L., Chazette, P., Gibert, F., Royer, P., et al. (2012). Spatio-temporal variability of the atmospheric boundary layer depth over the Paris agglomeration: An assessment of the impact of the urban heat island intensity. *Atmospheric Environment*, *63*, 261–275. <https://doi.org/10.1016/j.atmosenv.2012.09.046>
- Pataki, D. E., Alig, R. J., Fung, A. S., Golubiewski, N. E., Kennedy, C. A., McPherson, E. G., et al. (2006). Urban ecosystems and the North American carbon cycle. *Global Change Biology*, *12*(11), 2092–2102. <https://doi.org/10.1111/j.1365-2486.2006.01242.x>
- Peylin, P., Baker, D., Sarmiento, J., Ciais, P., & Bousquet, P. (2002). Influence of transport uncertainty on annual mean and seasonal inversions of atmospheric CO₂ data. *Journal of Geophysical Research*, *107*(D19), 4385. <https://doi.org/10.1029/2001jd000857>
- Pisso, I., Patra, P., Takigawa, M., Machida, T., Matsueda, H., & Sawa, Y. (2019). Assessing Lagrangian inverse modelling of urban anthropogenic CO₂ fluxes using in situ aircraft and ground-based measurements in the Tokyo area. *Carbon Balance and Management*, *14*(1), 1–23. <https://doi.org/10.1186/s13021-019-0118-8>
- Potosnak, M. J., Wofsy, S. C., Denning, A. S., Conway, T. J., Munger, J. W., & Barnes, D. H. (1999). Influence of biotic exchange and combustion sources on atmospheric CO₂ concentrations in New England from observations at a forest flux tower. *Journal of Geophysical Research*, *104*(D8), 9561–9569. <https://doi.org/10.1029/1999jd900102>
- Rayner, P. J., Enting, I. G., Francey, R. J., & Langenfelds, R. (1999). Reconstructing the recent carbon cycle from atmospheric CO₂, δ¹³C and O₂/N₂ observations. *Tellus B: Chemical and Physical Meteorology*, *51*(2), 213–232. <https://doi.org/10.1034/j.1600-0889.1999.t01-1-00008.x>
- Rayner, P. J., Law, R. M., Allison, C. E., Francey, R. J., Trudinger, C. M., & Pickett-Heaps, C. (2008). Interannual variability of the global carbon cycle (1992–2005) inferred by inversion of atmospheric CO₂ and δ¹³CO₂ measurements. *Global Biogeochemical Cycles*, *22*(3). <https://doi.org/10.1029/2007gb003068>
- Rayner, P. J., Utembe, S. R., & Crowell, S. (2014). Constraining regional greenhouse gas emissions using geostationary concentration measurements: A theoretical study. *Atmospheric Measurement Techniques*, *7*(10), 3285–3293. <https://doi.org/10.5194/amt-7-3285-2014>
- Rella, C. W., Chen, H., Andrews, A. E., Filges, A., Gerbig, C., Hatakka, J., et al. (2013). High accuracy measurements of dry mole fractions of carbon dioxide and methane in humid air. *Atmospheric Measurement Techniques*, *6*(3), 837–860. <https://doi.org/10.5194/amt-6-837-2013>
- Roest, G. S., Gurney, K. R., Miller, S. M., & Liang, J. (2020). Informing urban climate planning with high resolution data: The Hestia fossil fuel CO₂ emissions for Baltimore, Maryland. *Carbon Balance and Management*, *15*(1), 1–16. <https://doi.org/10.1186/s13021-020-00157-0>
- Seibert, P., & Frank, A. (2004). Source-receptor matrix calculation with a Lagrangian particle dispersion model in backward mode. *Atmospheric Chemistry and Physics*, *4*(1), 51–63. <https://doi.org/10.5194/acp-4-51-2004>
- Seto, K. C., Dhakal, S., Bigio, A., Blanco, H., Delgado, G. C., Dewar, D., et al. (2014). Human settlements, infrastructure and spatial planning.
- Skamarock, W. C., Klemp, J. B., Dudhia, J., Gill, D. O., Barker, D. M., Wang, W., et al. (2008). *2005: A description of the advanced research WRF version 2*. In *NCAR Tech. Note*.
- Staufer, J., Broquet, G., Bréon, F. M., Puygrenier, V., Chevallier, F., Xueref-Rémy, I., et al. (2016). The first 1-year-long estimate of the Paris region fossil fuel CO₂ emissions based on atmospheric inversion. *Atmospheric Chemistry and Physics*, *16*(22), 14703–14726. <https://doi.org/10.5194/acp-16-14703-2016>
- Super, I., Dellaert, S. N., Tokaya, J. P., & Schaap, M. (2021). The impact of temporal variability in prior emissions on the optimization of urban anthropogenic emissions of CO₂, CH₄ and CO using in-situ observations. *Atmospheric Environment: X*, *11*, 100119. <https://doi.org/10.1016/j.aea.2021.100119>
- Super, I., van der Gon, H. D., Visschedijk, A. J. H., Moerman, M. M., Chen, H., Van der Molen, M. K., & Peters, W. (2017). Interpreting continuous in-situ observations of carbon dioxide and carbon monoxide in the urban port area of Rotterdam. *Atmospheric Pollution Research*, *8*(1), 174–187. <https://doi.org/10.1016/j.apr.2016.08.008>
- Tarantola, A. (1987). Inversion of travel times and seismic waveforms. *Seismic tomography*, 135–157. https://doi.org/10.1007/978-94-009-3899-1_6
- Tarantola, A. (2005). *Inverse problem theory and methods for model parameter estimation*. Society for Industrial and Applied Mathematics.
- Turnbull, J. C., Miller, J. B., Lehman, S. J., Tans, P. P., Sparks, R. J., & Southon, J. (2006). Comparison of ¹⁴CO₂, CO, and SF₆ as tracers for recently added fossil fuel CO₂ in the atmosphere and implications for biological CO₂ exchange. *Geophysical Research Letters*, *33*(1), L01817. <https://doi.org/10.1029/2005gl024213>
- Turnbull, J. C., Sweeney, C., Karion, A., Newberger, T., Lehman, S. J., Tans, P. P., et al. (2015). Toward quantification and source sector identification of fossil fuel CO₂ emissions from an urban area: Results from the INFLUX experiment. *Journal of Geophysical Research: Atmospheres*, *120*(1), 292–312. <https://doi.org/10.1002/2014jd022555>
- Uliasz, M. (1994). Lagrangian particle dispersion modeling in mesoscale applications. *Somatosensory & Motor Research*, *760*, 23.
- van der Gon, H. D. (2019). Emissions and natural fluxes Dataset.
- Velders, G. J., Fahey, D. W., Daniel, J. S., McFarland, M., & Andersen, S. O. (2009). The large contribution of projected HFC emissions to future climate forcing. *Proceedings of the National Academy of Sciences*, *106*(27), 10949–10954. <https://doi.org/10.1073/pnas.0902817106>
- Vimont, I. J., Turnbull, J. C., Petrenko, V. V., Place, P. F., Sweeney, C., Miles, N., et al. (2019). An improved estimate for the δ¹³C and δ¹⁸O signatures of carbon monoxide produced from atmospheric oxidation of volatile organic compounds. *Atmospheric Chemistry and Physics*, *19*(13), 8547–8562. <https://doi.org/10.5194/acp-19-8547-2019>
- Wehr, R., Munger, J. W., Nelson, D. D., McManus, J. B., Zahniser, M. S., Wofsy, S. C., & Saleska, S. (2013). Long-term eddy covariance measurements of the isotopic composition of the ecosystem-atmosphere exchange of CO₂ in a temperate forest. *Agricultural and Forest Meteorology*, *181*, 69–84. <https://doi.org/10.1016/j.agrformet.2013.07.002>

- Wong, K. W., Fu, D., Pongetti, T. J., Newman, S., Kort, E. A., Duren, R., et al. (2015). Mapping CH₄: CO₂ ratios in Los Angeles with CLARS-FTS from mount Wilson, California. *Atmospheric Chemistry and Physics*, *15*(1), 241–252. <https://doi.org/10.5194/acp-15-241-2015>
- Yadav, V., Ghosh, S., Mueller, K., Karion, A., Roest, G., Gourdj, S. M., et al. (2021). The impact of COVID-19 on CO₂ emissions in the Los Angeles and Washington DC/Baltimore metropolitan areas. *Geophysical Research Letters*, *48*(11), e2021GL092744. <https://doi.org/10.1029/2021gl092744>
- Yver-Kwok, C., Philippon, C., Bergamaschi, P., Biermann, T., Calzolari, F., Chen, H., et al. (2021). Evaluation and optimization of ICOS atmosphere station data as part of the labeling process. *Atmospheric Measurement Techniques*, *14*(1), 89–116. <https://doi.org/10.5194/amt-14-89-2021>